

Experimental characterization of the opposition surge in fine-grained water–ice and high albedo ice analogs



B. Jost^{a,*}, A. Pommerol^a, O. Poch^b, B. Gundlach^c, M. Leboeuf^d, M. Dadras^d, J. Blum^c, N. Thomas^a

^a Physikalisches Institut, Universität Bern, Sidlerstrasse, 5, CH-3012 Bern, Switzerland

^b Center for Space and Habitability, Universität Bern, Sidlerstrasse, 5, CH-3012 Bern, Switzerland

^c Institut für Geophysik und Extraterrestrische Physik, Technische Universität Braunschweig, Mendelssohnstr. 3, D-38106 Braunschweig, Germany

^d Centre Suisse d'Electronique et Microtechnique (CSEM), Rue Jaquet-Droz 1, 2002 Neuchâtel, Switzerland

ARTICLE INFO

Article history:

Received 8 August 2014

Revised 15 September 2015

Accepted 15 September 2015

Available online 25 September 2015

Keyword:

Photometry

Experimental techniques

Ices

ABSTRACT

We measured the bidirectional reflectance in the VIS–NIR spectral range of different surfaces prepared from small-grained spherical water–ice particles over a wide range of incidence and emission geometries, including opposition. We show that coherent backscattering is dominating the opposition effect on fresh sample material, but its contribution decreases when particles become more irregularly shaped and the bulk porosity increases. Strong temporal evolution of the photometric properties of icy samples, caused by particle sintering and resulting in a decrease of backscattering, is shown. The sintering of the ice particles is documented using cryo-SEM micrographs of fresh and evolved samples. To complement the photometric characterization of ices, multiple high albedo laboratory analogs were investigated to study the effects of shape, grain size distribution, wavelength and surface roughness. In addition to the main backscattering peak, the phase curves also display the effect of glory in the case of surfaces of granular surfaces formed by either spherical ice or glass particles. We show that the angular position of the glory can be used to determine accurately the average size of the particles. Reflectance data are fitted by the Hapke photometric model, the Minnaert model and three morphological models. The resulting parameters can be used to reproduce our data and compare them to the results of other laboratory experiments and astronomical observations.

© 2015 Elsevier Inc. All rights reserved.

1. Introduction

The reflectivity of a granular surface depends on numerous parameters such as the chemical composition, the internal structure of the grains, the particle size distribution, porosity and surface topography. The direction of the incident light and the direction of observation also have a strong influence on the measured reflectivity. Brightness variations of a surface caused by changing illumination and observation geometries are commonly characterized by phase curves where the phase angle, α , is the angle between the illumination and observation directions as seen from the surface.

A ubiquitous and particularly interesting phenomenon observed in measured phase curves is the so-called “opposition effect”, a sharp, nonlinear surge in brightness when the directions of illumination and observation become nearly parallel (i.e. the

phase angle goes to 0°). It is an omnipresent feature that has been observed on many kinds of objects including planetary and terrestrial terrains, planetary rings, asteroids, as well as laboratory samples (see e.g. Helfenstein et al., 1997 or Déau et al., 2013).

The opposition effect was first described by Seelinger (1884) and Müller (1885), who analyzed brightness measurements of the rings of Saturn. More recent reviews of the opposition effect in the Solar System and its mechanisms can be found in Rosenbush et al. (2002) and Belskaya et al. (2008). According to a generally accepted view, this peak can be caused by two different mechanisms: Shadow Hiding Opposition Effect (SHOE, e.g. Seelinger, 1887; Hapke, 1986) and Coherent Backscattering Opposition Effect (CBOE, e.g. Wolf and Maret, 1985; Tsang and Ishimaru, 1985; Muinonen et al., 2012). When particles are much larger than the wavelength of the light, an illuminated surface is partially covered by shadows when observed at larger phase angles, whereas at opposition the entire surface observed is illuminated and shadows disappear, which noticeably increases its brightness (Hapke, 2002). When the particles are in the same range of size as the wavelength, the grains cannot create a well-defined

* Corresponding author at: Physikalisches Institut, Universität Bern, Sidlerstrasse, 5, CH-3012 Bern, Switzerland.

E-mail address: bernhard.jost@space.unibe.ch (B. Jost).

shadow, because of the wave-nature of light. At this scale, the CBOE dominates the opposition effect (Liang and Mishchenko, 1997). CBOE occurs as well on complex shaped large grains, because microscopic grain-surface irregularities, voids and inclusions are of much smaller scale than the dimension of the entire particle and therefore allow multiple scattering (Shkuratov and Helfenstein, 2001; Hapke, 2002). CBOE can be understood as a constructive interference of two rays, coming from the same direction, but undergoing the same scattering path between particles in the opposite direction. At exactly zero phase angle they would be in phase and interfere constructively. This is independent of spatial proximity between the two rays, but only because they had the same origin (Akkermans et al., 1986). The angular half-width of the CBOE is always much narrower than the one of SHOE, e.g. in case of the lunar regolith $\sim 2^\circ$ versus $\sim 8^\circ$ (Hapke et al., 1998). Contrary to the SHOE, the angular width and the amplitude of CBOE should positively correlate to the wavelength in case of visible light and particles sizes in the micrometer-range (Van Albada et al., 1990; Mishchenko, 1992; Hapke et al., 1998, 2012; Hapke, 2002). Discussion about correlations between sample material properties and the opposition effect can be found in Shkuratov et al. (2002) or Muinonen et al. (2002).

The “normal reflectance” of planetary surfaces, which can be mapped by laser altimeters, as a side product of the determination of the surface topography (Gardner, 1982; Thomas et al., 2007) is strongly influenced by both the SHOE and CBOE. The intensity of the opposition peak is therefore a crucial parameter for dimensioning these instruments. A good understanding of the physical and compositional parameters that control the opposition effect is also required to interpret the spatial variations of the reflectance observed at the surface. The characterization of the opposition effect in icy surfaces is particularly relevant for the preparation of the GAnymede Laser Altimeter (GALA; Hussmann et al., 2013) experiment on-board ESA's upcoming JUICE mission (Grasset et al., 2012) to be launched in 2022 toward the jovian system.

Another interesting optical scattering phenomenon discussed in the present work is the glory. It is often seen from airplanes as a concentric rainbow-like feature around the plane's shadow cast on a cloud layer (see Laven, 2005a). It has also been already observed in the laboratory on bidirectional reflectance measurements of samples consisting of glass beads (Shkuratov et al., 2002; Hapke et al., 2009). Recently, evidence for glory on venusian cloud tops was obtained by the Venus Monitoring Camera (VMC) of ESA's Venus Express mission. Useful information on the composition and particle size of the clouds could be derived from this observation (Markiewicz et al., 2014). To our knowledge, there is no report in the literature of the observation of glory on icy surfaces, although Hapke (1993) notes that glory can contribute to the opposition effect if samples are composed of spherical particles. Glory originates from the interaction of light rays propagating along different optical paths inside transparent spherical.

Although Mie theory (Mie, 1908) can simulate glories accurately, it offers no precise explanation for their formation. Laven (2005b) used simulations with the Debye series to suggest that glories are a result of two-ray interference between two surface waves with a phase difference. The glory effect depends on the particle size parameter, i.e. the ratio of the scattering particle size and the wavelength. For visible light, it is restricted to particle diameters between 8 and 50 μm (Laven, 2005a). Furthermore, broad size distributions ($\sigma > 2 \mu\text{m}$) have the effect of smearing the primary peak and vanishing secondary maxima. There is no simple formula for the relationship between particle size and angular separation of the first maximum. Mayer et al. (2004) determined water cloud droplet sizes and distribution from remote sensing observations made by the Compact Airborne

Spectrographic Imager (CASI) by fitting numerical models to their data. They proved that the technique was reliable for deriving the effective radius and the width of the size distribution, but not its exact shape.

Contrary to the opposition effect, the glory effect is a phenomenon purely originating from the single particle scattering phase function and restricted to spherical particles. The parallel observation of the glory and CBOE on a sample indicates that, at distinct phase angles, the single scattering mechanism dominates over the multiple scattering (scattering between particles), which is necessary for coherent backscattering.

There is little laboratory data available on the photometry of different types of icy surfaces and especially in opposition geometry, whereas numerous observations of icy surfaces in the outer Solar System have already been obtained (e.g. Kaasalainen et al., 2001; Rosenbush et al., 2002; Verbiscer et al., 2013). In a previous work, we characterized micrometer-sized spherical water-ice particles (Gundlach et al., 2011; Gundlach and Blum, 2015) and measured their phase curves at phase angles between 5° and 130° (Jost et al., 2013). These particles are thought to be representative analogs for some icy surfaces in the outer Solar System. To be able to measure such samples at low phase angles, the PHIRE-2 goniometer (Pommerol et al., 2011) of the University of Bern has been modified. A system with a beam splitter was constructed to observe at geometries where the detecting unit was vignetting the incoming light in the previous setup.

Several goniometers have been built in the past decades or are presently under construction, to measure bidirectional reflectance. For example the long-arm goniometer at JPL in Pasadena (Nelson et al., 2000), the spectro-goniometer in Grenoble (Brissault et al., 2004), PHIRE-1 in Bern (Gunderson et al., 2006), the Bloomsburg University Goniometer (BUG; Shepard and Helfenstein, 2007), ISEP in Toulouse (Souçon et al., 2011), and unnamed instruments in Helsinki (Kaasalainen et al., 2002; Näränen et al., 2004) and Kharkov (Shkuratov et al., 2002; Psarev et al., 2007).

All of them have certain advantages and drawbacks in terms of maximum/minimum phase angle, temperature range, spectral range and resolution, angular resolution or acquisition speed, as it is not possible to optimize all these parameters in one single experiment.

There are only a few studies of high albedo laboratory analogs in opposition geometry or at low phase angles. A very extensive study of structural analogs for planetary regoliths was performed by Shkuratov et al. (2002), including magnesium oxide, aluminum oxide, glass beads, hollow glass spheres, silica and terrestrial snow. The authors investigated effects of albedo, bulk compression, particle size, wavelength and particle shape on the opposition effect and degree of polarization. Hapke et al. (2009) characterized soda-lime glass microspheres at BUG and JPL. Nelson et al. (2000) and Kaasalainen (2003) investigated aluminum oxide particles. Deb et al. (2011) also measured aluminum oxide but at large phase angles.

In this work, we present a variety of bidirectional reflectance measurements on high albedo materials, including spherical ice particles, with different surface preparations. Reflectance was measured over a range of large phase angle including the opposition geometry. We demonstrate how particle size, macroscopic roughness, and wavelength influence the bidirectional reflectance properties. We further characterize the temporal evolution of fine-grained ice particles as a follow-up work of Jost et al. (2013) and prove the sintering hypothesis postulated therein by imaging samples composed of micrometer-sized water ice particles with a cryogenic scanning electron microscope. Furthermore we present a method to characterize the particle sizes directly from the measured phase curves.

2. Methods

2.1. Photometric measurements

2.1.1. Instrument

All the data presented in this article were acquired with the PHIRE-2 (Physikalisches Institut Radiometric Experiment-2) radio-goniometer, the same instrument used in our previous work (Pommerol et al., 2013; Jost et al., 2013) but with significant technical improvements. We will only describe here the aspects of the instrument that are directly relevant for this study. The instrument specifications are summarized in Table 1. For additional details on the instrument, see Pommerol et al. (2011).

PHIRE-2 is a radio-goniometer with two mobile arms placed in a large freezer. It can be operated either at ambient conditions or at subzero temperature (minimum -35°C). The longer arm holds the light source and its position is described by the incidence angle, i . The shorter arm holds an optical deflection system to conduct the light reflected from the sample to a Si photodiode. Its position is described by the emission angle, e , and the azimuth angle, α . The angle between the incidence and emission directions is the “phase angle” α . The vertical plane containing the incidence direction is called the “principal plane”. In this study, all measurements were acquired in the principal plane, keeping the azimuth angle fixed at 0° , as all of our samples are assumed to be highly isotropic. Furthermore our volatile icy samples demand a high acquisition speed, so the restriction to the principal plane was a compromise. The angles can then be represented schematically as in Fig. 1.

The PHIRE-2 instrument permits measurements of photometric properties in the spectral range: 400–1100 nm. To reach the maximum angular resolution, the diameter of the illuminated spot on the sample is reduced to 5 mm with an iris diaphragm. This way, a theoretical angular resolution of 0.46° is achieved, as defined by the spot size, the aperture size of the optical fiber at the entrance of the detector and the lengths of the arms. Thus we use angular steps of 0.5° to characterize the sharp peak around

Table 1
Specifications of the PHIRE-2 radio-goniometer.

Goniometer specifications						
Operating temperature	−35 to +25 °C					
Operating pressure	Ambient atmosphere					
Optical filters						
Wavelength (nm)	450	550	650	750	905	1064
FWHM (nm)	70	70	70	70	10	10
Relative signal strength (%)	10	30	69	100	39	15
Light source	250 W tungsten-halogen					
Energy input	<5 μW/cm ²					
Illuminated spot size	5–20 mm (adjustable with an iris)					
Angular resolution	0.5° (with 5 mm spot size)					
Observation phase angle	0–150°					

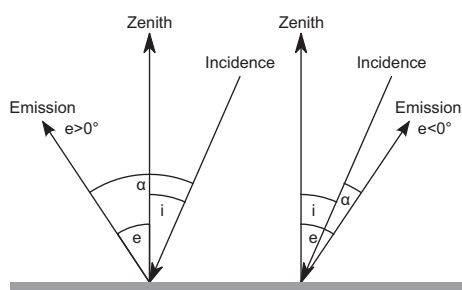


Fig. 1. Definition of photometric angles in the experimental setup. The incidence angle, i , is always positive. The left graph shows the configuration for positive emission angle, the right is for negative emission angles.

the opposition ($\alpha < 5^{\circ}$), whereas a step size of 5° is used at larger phase angles.

The most important hardware modification compared to our previous work is the use of a beam splitter system on the detector arm (Fig. 2) to allow us to perform measurements at low phase angles, including the opposition ($\alpha = 0^{\circ}$). This technical solution was inspired by a previous development on the PHIRE instrument (Gunderson and Thomas, 2008). The beam splitter is a $50 \times 100 \times 3$ mm fused silica plate with multilayer coatings on both sides. Its width of 100 mm permits reflectance measurements for phase angles up to 5° on each side of the incidence direction. The custom-made coating, realized by Cosmo Optics (Middletown, NY, USA), is optimized for a Reflection to Transmission (R/T) beam-splitting ratio of $R/T = 50/50$ over the 350–1100 nm spectral range at a nominal angle of incidence of 45° , with minimum sensitivity to polarization.

In addition to the multilayer-coated beam splitter, we acquired some measurements with a so-called “polka-dot” beam splitter. This type of beam splitter consists of a chessboard-like reflective pattern of aluminum coating deposited on a substrate of fused silica. The spacing between the square-shaped reflective areas is $109\ \mu\text{m}$. The main advantage of this type of beam splitter is that it displays a perfectly constant beamsplitting ratio over the whole spectral range and is insensitive to polarization. The drawback, however, is that it produces strong scattering of the transmitted light as well as significant diffraction. The scattering is responsible for high levels of straylight hitting the detector, preventing its use for measurements of dark samples. The diffraction by the small square apertures causes a cross-shaped spreading of the light spot onto the sample. Measurements with the polka-dot beam splitter are thus restricted to large and bright samples. They are however invaluable as complementary measurements to the multi-layer coated beam splitter and ensure that spectral and polarization effects in the multilayer coating data can be assessed. Except Fig. 3, this work shows only data acquired with the multilayer-coated beam splitter. A summary of specifications is given in Table 2.

The beam splitter is mounted into a frame that holds it at a tilt angle of 45° from the illumination direction (Fig. 2). A deflection plate covered with a neutral density filter (4.0 optical density) is mounted in front of the beam splitter with an angle of 100° . It absorbs the vast majority of the light reflected by the beam splitter and reflects the rest specularly toward the back wall of the freezer, which is painted with a very absorbing paint.

To complement this beam splitter head, we built a narrow head with a 1-in. silver-coated mirror, which permits measurements down to a minimum phase angle of 3° . We can therefore acquire data with both systems between $\alpha = 3^{\circ}$ and $\alpha = 5^{\circ}$. This overlap is necessary to calibrate the beam splitter system properly at geometries where the beam passes through the beam splitter. The two heads are easily and quickly exchangeable. They both have fine alignment mechanisms that are used to align the heads with the rest of the instrument. Once this has been done, no more alignment is required after an exchange of the heads.

To further test the reliability of our new zero-phase-angle setup and the associated data reduction procedures, we re-measured a sample of glass bubbles (see Table 3). This material behaves almost like a fluid and does not form agglomerates. Is therefore very insensitive to variations in surface preparation. In Fig. 3 we show the good agreement between the phase curves acquired with the mirror head and the two new beam splitter heads at $\alpha > 5^{\circ}$ and with the two beam splitter heads at $\alpha < 5^{\circ}$.

2.1.2. Calibration

The radio-goniometer equipped with the beam splitter head (Fig. 2) is a much more complex optical system than when it is

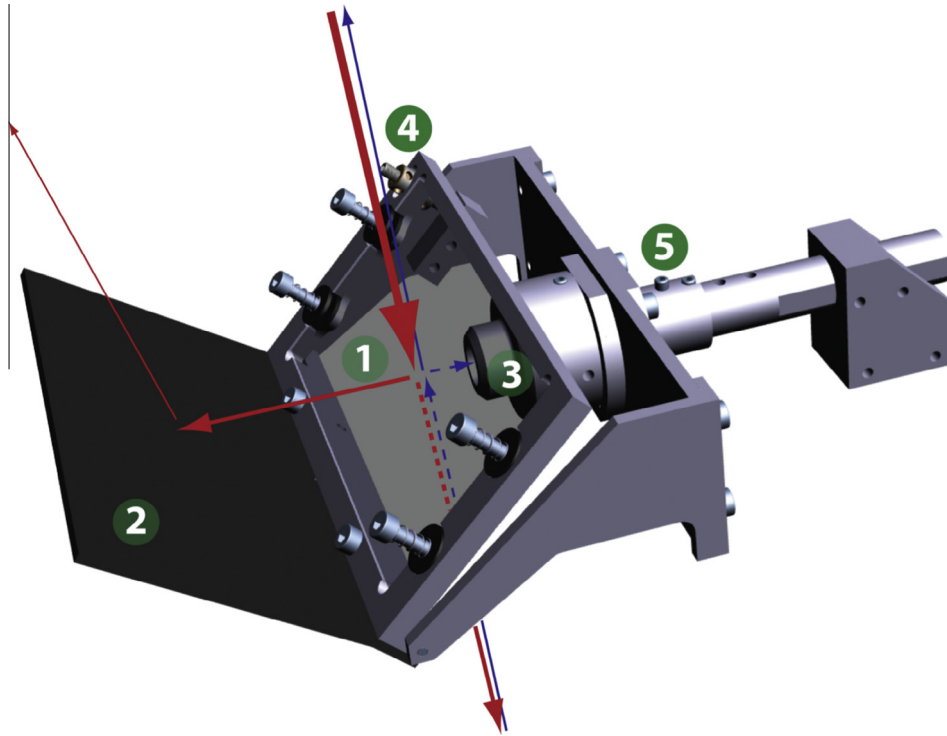


Fig. 2. CAD view of the beam splitter head. The incoming light (largest red arrow) is split up: 50% is transmitted through the beam splitter (1) toward the sample while the other 50% is reflected toward the deflection plate (2) where most of it is absorbed by a neutral density filter and the remaining is reflected. The light scattered from the sample (indicated in blue) is again partly reflected by the beam splitter (1). One fraction reaches the fiber (3), which leads to the detector, while another part is transmitted in the illumination direction. A mechanism allows us to precisely adjust the orientation of the beam splitter (4) during alignment. A quick release mechanism (5) allows us to rapidly exchange the beam splitter head and the mirror head on the PHIRE-2 instrument without re-aligning them. (For interpretation of the references to color in this figure legend, the reader is referred to the web version of this article.)

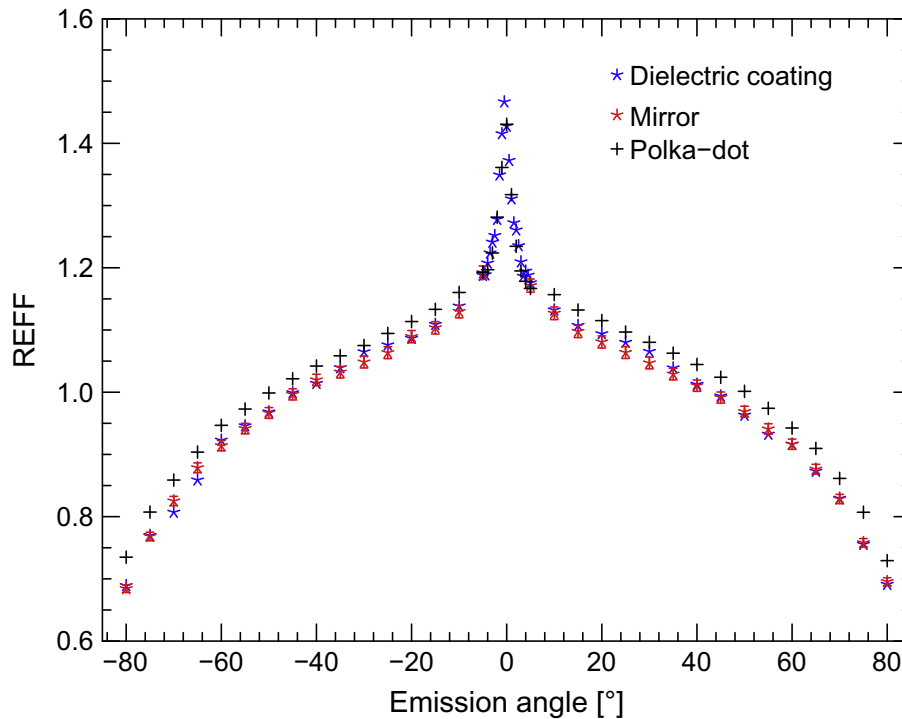


Fig. 3. Comparison of the phase curves measured with three different hardware setups of the PHIRE-2 experiment, to verify the functionality. Dielectric coating and polka-dot are two types of beam splitters with complementary advantages and drawbacks. The mirror head is limited to measurements at phase angles larger than 3°. The sample is a smooth surface made of glass bubbles (hollow borosilicate glass spheres, diameter: 10–100 μm , from 3MTM, see Table 3). The phase curves were measured for normal incidence ($i = 0^\circ$) and at a wavelength of 650 nm. A good agreement is observed between all these curves, which proves the accuracy of the particular calibration procedure implemented for measurements with the beam splitter head.

Table 2

Characteristics of different PHIRE-2 detector setups.

	Mirror	Polka-dot BS	Multilayer coating BS
Minimum phase angle (°)	4	0	0
Polarization effects	No	No	Yes
Spectral effects	No	No	Yes (42–57% R/T between 350 and 1100 nm in random polarization)
Signal to noise	Excellent	Weak	Satisfying
Optical artifacts	No	Diffraction	Negligible ghosting

Table 3

Material and preparation characteristics of non-volatile samples.

Sample	D (μm)	Shape	Surface preparation	Notes
Aluminum oxide abrasive (Microgrit WCA 1)	1.77–2.25 (50%) ^a	Flattened with sharp edges, smooth surfaces	Flattened with spatula/sprinkled with sieve	Formation of agglomerates
Sodium chloride	<80	Irregular	Flattened with spatula	Ground and sieved with 80 μm mesh-size
Sodium chloride	80–200	Irregular	Flattened with spatula	Ground and sieved with 80 μm and 200 μm mesh-size
Soda–lime–borosilicate glass bubbles (3M TM)	10–100	Hollow spheres	Flattened with spatula	Very low adhesion forces
Potter Spherglass 5000 (soda–lime glass)	0.5–19.3 (90%) ^a	Regular spheres	Flattened with spatula/sprinkled with sieve	Slight formation of agglomerates
Potter Spherglass 7010	0.5–10 (top cut of type 5000) ^a	Regular spheres	Flattened with spatula	Formation of agglomerates
Potter Spherglass 7025	10–19.3 ^a	Regular spheres	Flattened with spatula	Slight formation of agglomerates

^a Specified by manufacturer.

equipped with the mirror head. Two potential issues must be addressed and solved by careful and accurate characterization and calibration of the system: (1) the path of the incident light reflected by the beam splitter toward the deflection plate and (2) the scattered straylight produced by this reflection, which can reach the detector directly.

A fraction of the incident light that reaches the beam splitter is scattered in all directions, including the one of the detector fiber, located nearby. In the case of the polka-dot beam splitter, the straylight produced in this way reaches levels comparable to the signal reflected from the sample itself, restricting the measurements to bright samples. The scattering is significantly lower with the coated beam splitter and can, thus, be accurately calibrated, even when studying dark samples. However, because the scattering is essentially caused by the deposition of dust onto the window, the calibration must be done frequently (if possible every day and in any case before and after measurements of the sample to ensure that no large changes occurred). The straylight is characterized by acquiring reflectance measurements of a specular ND-filter (4.0 OD) in a non-specular geometry. These signal values are then subtracted from the signal measured with the sample datasets to eliminate artifacts from the optical system.

The absolute calibration is performed by normalizing the raw voltage signals to a single reflectance measurement of a white Spectralon reference (99% hemispheric reflectance) measured at $i = 0^\circ$ and $e = 55^\circ$ according Eq. (1) (see Gunderson et al., 2007). This procedure can be used for the mirror and the beam splitter system. It is performed for the mirror and beam splitter separately.

$$C_i = 0.99 * \frac{\cos(e = 55^\circ)}{\pi * V_{55} * \cos(i = 0^\circ)} [\text{sr}^{-1} \text{V}^{-1}] \quad (1)$$

To calibrate the geometries where the beam passes the beam-splitter ($\alpha < 6^\circ$), the values of the beam splitter curve are multiplied by an empirical constant factor, which is about 2.1 and slightly wavelength dependent. This is performed so that the brightness at $\alpha = 4^\circ$ and 5° is identical for both setups.

By using this method, we obtain data calibrated in units of the radiance factor (RADF) that we systematically convert to “reflectance factor” (REFF). The reflectance factor was defined by Hapke (1993) as the ratio between the actual reflectance of the sample measured in a particular geometry and the one of a hypothetical perfect Lambertian diffuser observed in the same geometry. Conversion from radiance to reflectance factor is simply achieved by dividing the radiance factor by the cosine of the incidence angle, $\text{REFF} = \text{RADF}/\cos(i)$. The reflectance factor REFF is related to the bidirectional reflectance r , radiance I [$\text{W m}^{-2} \text{sr}^{-1}$], irradiance F [W m^{-2}] and to the Bidirectional Reflectance Distribution Function (BRDF) as shown in Eq. (2).

$$\text{REFF} = \pi * \text{BRDF} = \pi * \frac{r}{\cos(i)} = \pi * \frac{I}{F * \cos(i)} \quad (2)$$

2.1.3. Measurement uncertainties

The mechanical accuracy of the PHIRE-2 instrument has been slightly improved compared to the measurements reported in Jost et al. (2013) by replacing gear wheels. The long-term (tens of hours) stability is still about 1%, mainly influenced by the stability of the light source and temperature variations. An accurate estimate of the measurement uncertainties can also be obtained from the data themselves by applying the reciprocity principle (see Eq. (10.9b) in Hapke, 1993) where pairs of measurement points are compared as the position of the source and detector are permuted. By definition, $\text{REFF}(i, e, \alpha)$ and $\text{REFF}(e, i, \alpha)$ should be identical. By comparing all possible combinations in one dataset, we obtain a robust estimation of the measurement errors. As opposed to simple stability measurements, this estimate takes into account most of the mechanical imperfections and optical misalignments. On samples with very high surface roughness the errors can reach values up to 15% because the illuminated spot area varies with illumination angle from round to ellipsoidal. In general it can be seen that errors are higher by a factor of about 2 at sub-zero temperature when vibrations generated by the compressor of the freezer influence the instrument.

2.1.4. Sample tilt correction

It is practically impossible to prepare perfectly flat and horizontal samples at the scale of the illuminated area. Even when they look perfectly even and horizontal by eye, the surfaces can be tilted by as much as 1° or 2° in some cases. Because our calibration includes the division of raw voltages by the cosines of the incidence and emission angles, small angle uncertainties result in non-negligible errors at large incidence and emission angles. We apply a first-order correction to mitigate this effect, by assuming a perfectly flat surface but tilted from the horizontal plane. An automatized procedure compares the symmetry at normal illumination and calculates the angular misalignment. The optical reference system is then rotated by this angle as the new “vertical” position. This is done for every sample.

The second correction step is performed during the data calibration. Different reflectance values are compared to the corresponding set of measurement in the opposite emission direction. The best tilt correction is found by optimizing the value of tilt angle to minimize the asymmetry.

2.1.5. Measurement sequences

The standard measurement procedure used here consists of scanning with the detector arm from $e = -80^\circ$ to $e = +80^\circ$ for a fixed incidence direction (this takes about 6 min). After having measured all different incidence angles, the bandpass filter is changed and the procedure repeated. Due to different combinations of incidence directions and wavelengths, the total time needed for data acquisition can vary from some minutes to several hours. This combination is called a “sequence” in the following sections.

To characterize the evolution of the bidirectional reflectance of volatile sample materials such as ice, the complete sequence is repeated multiple times.

2.2. Cryogenic SEM

The particle sizes and microscopic structure of ice and other analogs were investigated with a cryogenically-cooled scanning electron microscope (SEM) at Centre Suisse d'Electronique et Microtechnique (CSEM) in Neuchatel. The microscope is a Philips XL30 ESEM-FEG, operated at 5 kV and a chamber pressure of $<10^{-4}$ mbar. The cryotransfer system is a Gatan Alto 2500. Inside the cryotransfer system the sample material was sputter-coated with some nanometers of platinum to render it conducting.

2.3. Photometric modeling

2.3.1. Hapke model

We used the Hapke photometric model (Hapke, 1993, 2002), which is the most popular model in planetary remote-sensing, to fit our data. This model attempts to relate the optical properties of single particles (single scattering albedo and single scattering phase function) with the bidirectional reflectance of a surface composed of such particles by considering light scattering between particles and the influences of macroscopic parameters such as porosity and surface roughness.

For our work we used the Isotropic Multiple Scattering Approximation (IMSA), from (Hapke, 1993) but with a new analytic approximation of the Ambartsumian–Chandrasekhar H-function and CBOE (Hapke, 2002). For the Henyey–Greenstein (HG) function we follow the definition used by McGuire and Hapke (1995), of a two-term HG function where b is the shape parameter and c is the backscattering parameter. A particle is mostly forward scattering when $c < 0$ and backscattering when $c > 0$.

It is not the aim of this work to discuss the applicability or physical meaning of the Hapke photometric model. We use it here to

provide an easy way to reproduce and extrapolate our experimental data. The fitted parameters can be found in Table 4.

2.3.1.1. Fitting technique and error estimation. We used the same two-step fitting procedure as in our previous publications (Jost et al., 2013; Pommerol et al., 2013), a combined use of a Particle Swarm Optimization (PSO) strategy (Kennedy and Eberhart, 1995) and a Levenberg–Markwardt algorithm (MPFIT, Markwardt, 2008).

The goodness of the fit is expressed in the usual way by the total and reduced chi-square, χ^2 and χ^2_{red} , respectively.

To obtain uncertainties on individual parameters, we use a similar method as Johnson et al. (2006) to establish a 1σ confidence interval. Starting from an optimum set of model parameters, one parameter is taken and varied in incremental steps in the complete parameter space while the others are re-fitted to compensate for the deviation. If the resulting χ^2 -curve has a clear minimum, then the parameter is well constrained. A 1σ confidence interval is defined by the two points around the minimum where the curve reaches $\chi^2_{min} + \Delta\chi^2_{1\sigma}$ (Gunderson et al., 2007). In our case of a model with 7 degrees of freedom, $\chi^2_{1\sigma} = 8.18$, (which is the χ^2 -critical-value when the cumulative probability of the χ^2 distribution is $1\sigma = 0.68$).

2.3.2. Minnaert model

The empirical Minnaert model (Minnaert, 1941) relates the dependence of reflectance to scattering geometry, i , e and α . In units of reflectance factor it has the form

$$\text{REFF}(i, e, \alpha) = A(\alpha) [\cos(i) \cos(e)]^{k(\alpha)-1} \quad (3)$$

$A(\alpha)$ is commonly called the Minnaert-albedo, $k(\alpha)$ is the Minnaert-limb-darkening parameter. Both depend on phase angle. Values of $k(\alpha) > 0.5$ indicate limb darkening. To describe $A(\alpha)$ we use an empiric linear function in magnitude with a phase slope parameter, β in mag/deg, and the Minnaert-albedo at opposition, A_0 , which is equivalent to normal albedo. This function was previously introduced by Li et al. (2013), it has the form

$$A(\alpha) = A_0 10^{0.4\beta\alpha} \quad (4)$$

As it cannot account for the opposition surge, the fit of $A(\alpha)$ is performed on the interval $\alpha = [5^\circ, 60^\circ]$. The k parameter is described as well by a linear function, as suggested by McEwen (1991),

$$k(\alpha) = k_0 + b\alpha \quad (5)$$

with a slope b , in deg^{-1} . To fit $k(\alpha)$, phase angles between 0° and 100° are considered. The modeled parameters can be found in Table 5.

2.3.3. Morphological parameters

To express the shape of our phase curves with morphological parameters, we used the linear model of Lumme and Irvine (1976) in its original form and a normalized form that should be correct for the non-zero angular size of the light source.

The Lumme & Irvine model consists of two linear functions:

$$r_{lin}(\alpha < 2.5^\circ) = A_0\alpha + B_0 \quad (6)$$

$$r_{lin}(\alpha > 10^\circ) = A_1\alpha + B_1 \quad (7)$$

The morphology parameters are defined as:

$$A = \frac{B_0}{B_1}, \quad \text{WHHM} = \frac{(B_0 - B_1)}{2(A_0 - A_1)} \quad \text{and} \quad S = -A_1 \quad (8)$$

The amplitude A is dimensionless. The half-width at half-maximum (WHHM) has units of degrees and the slope S has a unit of

Table 4

Hapke parameters of selected datasets in this work. Fitted with the 2002-version and a 2-parameter HG function. The confidence intervals are calculated as described in Section 2.3.1.1. The asymmetry parameter g is derived from b and c .

Sample	λ (nm)	χ^2_{red}	ω_0	+	−	$\bar{\theta}$	+	−	h_s	+	−	B_s	+	−	h_c	+	−	B_c	+	−	b	+	−	c	+	−	g
Aluminum oxide (flat)	650	2.44	1.000	0.000	0.005	0.5	1.5	0.5	0.30	0.06	0.05	1.00	0.00	0.06	0.03	0.01	0.01	0.32	0.03	0.03	0.28	0.02	0.02	−0.71	0.03	0.03	−0.28
Aluminum oxide (rough)	650	5.21	0.985	0.005	0.005	8.0	0.5	0.5	1.00	0.00	0.05	0.78	0.08	0.07	0.04	0.01	0.01	0.19	0.01	0.01	0.35	0.02	0.01	1.35	0.01	0.01	−0.35
Salt <80 μm	650	2.93	1.000	0.000	0.005	0.5	2.0	0.5	0.01	0.01	0.01	0.52	0.06	0.06	0.01	0.01	0.01	0.01	0.01	0.01	0.23	0.01	0.02	−0.10	0.04	0.03	−0.23
Salt 80–200 μm	650	1.32	1.000	0.000	0.005	1.5	1.5	1.5	0.99	0.01	0.04	0.38	0.10	0.11	0.02	0.01	0.01	0.03	0.02	0.01	0.24	0.02	0.03	−0.47	0.05	0.05	−0.24
Spherglass 7010 (rough)	750	1.39	0.985	0.005	0.005	0.5	5.0	0.5	0.09	0.04	0.01	0.76	0.01	0.09	0.02	0.02	0.01	0.05	0.01	0.04	0.24	0.03	0.04	1.26	0.13	0.09	−0.24
Spherglass 5000 (rough)	750	0.65	0.995	0.005	0.005	6.0	2.0	6.0	0.05	0.04	0.02	0.99	0.01	0.08	0.07	0.20	0.07	0.08	0.08	0.07	0.35	0.05	0.05	0.05	0.11	0.11	−0.35
Spherglass 7025 (rough)	750	2.51	0.995	0.005	0.005	4.0	1.5	4.0	0.07	0.04	0.02	0.99	0.01	0.13	0.25	0.09	0.09	0.20	0.05	0.04	0.30	0.03	0.03	−0.09	0.05	0.05	−0.3
Spherglass 5000 (flat)	750	1.84	1.000	0.000	0.005	0.5	7.0	0.5	0.19	0.14	0.09	1.00	0.00	0.07	0.05	0.02	0.02	0.30	0.04	0.05	0.54	0.08	0.04	−0.81	0.04	0.05	−0.54
Glass bubbles	650	30.11	1.000	0.000	0.005	1.5	0.5	0.5	1.00	0.00	0.03	0.99	0.01	0.01	0.04	0.01	0.01	0.16	0.01	0.01	0.59	0.01	0.01	−0.82	0.01	0.02	−0.59
Ice Method #2 (10 min)	650	1.32	1.000	0.000	0.005	0.5	3.5	0.5	0.02	0.02	0.15	1.00	0.00	0.39	0.99	0.01	0.20	0.17	0.04	0.03	0.54	0.05	0.04	−0.97	0.01	0.03	−0.54
Ice Method #2 (3.20 h)	750	1.87	1.000	0.000	0.005	0.5	2.5	0.5	1.00	0.00	0.74	0.01	0.13	0.01	0.99	0.01	0.51	0.05	0.01	0.03	0.63	0.03	0.02	−0.93	0.02	0.06	−0.63
Ice Method #3 (5 min)	750	0.31	1.000	0.000	0.010	11.0	5.5	11.0	0.02	0.98	0.02	0.57	0.43	0.57	0.01	0.99	0.01	0.01	0.44	0.01	0.51	0.17	0.28	−0.16	0.70	0.50	−0.51
Ice Method #3 (4.40 h)	750	0.91	0.990	0.010	0.010	0.5	7.0	0.5	0.01	0.27	0.01	0.20	0.24	0.20	0.99	0.01	0.62	0.29	0.32	0.25	0.27	0.09	0.14	0.68	0.29	0.46	−0.27
Ice Method #1 (10 min)	750	0.56	1.000	0.000	0.010	11.0	3.5	11.0	1.00	0.00	0.99	1.00	0.00	0.55	0.05	0.95	0.05	0.22	0.01	0.22	0.21	0.25	0.13	−0.95	0.31	0.05	−0.21
Ice Method #1 (4.50 h)	750	0.91	1.000	0.000	0.005	12.5	2.5	4.5	1.00	0.00	0.64	1.00	0.00	0.32	0.03	0.12	0.03	0.15	0.13	0.10	0.17	0.11	0.08	−1.00	0.22	0.00	−0.17

Table 5

Fitted model parameters of selected datasets. The corresponding definitions can be found in Sections 2.3.2 and 2.3.3.

Sample	λ (nm)	Minnaert model parameters				Original morphology parameters						Normalized morphology parameters					
		A_0	β	k_0	b	A	ΔA	HWHM	Δ HWHM	S	ΔS	A'	$\Delta A'$	HWHM'	Δ HWHM'	S'	$\Delta S'$
Aluminum oxide (flat)	650	1.08	−0.0004	0.94	0.0032	1.23	0.01	1.55	0.19	0.0027	0.0002	1.56	0.02	4.33	0.18	0.0024	0.0002
Aluminum oxide (rough)	650	1.21	−0.0061	0.68	0.0038	1.17	0.01	1.76	0.28	0.0051	0.0002	1.61	0.01	4.03	0.13	0.0043	0.0002
Salt <80 μm	650	0.96	−0.0001	0.93	0.0029	1.05	0.01	1.11	0.29	0.0020	0.0001	1.18	0.01	3.62	0.25	0.0020	0.0001
Salt 80–200 μm	650	1.04	−0.0006	0.98	0.0022	1.03	0.01	0.75	0.37	0.0020	0.0002	1.14	0.01	3.41	0.54	0.0019	0.0002
Spherglass 7010 (rough)	750	1.00	−0.0047	0.72	0.0041	1.16	0.01	1.54	0.26	0.0037	0.0002	1.53	0.02	4.01	0.17	0.0037	0.0002
Spherglass 5000 (rough)	750	1.05	−0.0038	0.79	0.0042	1.20	0.03	1.65	0.49	0.0044	0.0004	1.69	0.03	4.13	0.28	0.0042	0.0004
Spherglass 7025 (rough)	750	1.04	−0.0056	0.79	0.0042	1.22	0.02	1.59	0.23	0.0046	0.0002	1.78	0.02	4.19	0.14	0.0045	0.0002
Spherglass 5000 (flat)	750	1.06	−0.0034	0.91	0.0044	1.24	0.02	1.71	0.29	0.0049	0.0003	1.79	0.02	4.18	0.16	0.0045	0.0003
Glass bubbles	650	1.13	−0.0013	0.94	0.0046	1.19	0.01	1.55	0.11	0.0044	0.0001	1.57	0.01	4.06	0.08	0.0037	0.0001
Ice Method #2 (10 min)	650	1.04	0.0004	1.03	0.0035	1.02	0.01	1.06	1.34	0.0039	0.0003	1.20	0.01	3.13	0.42	0.0035	0.0002
Ice Method #2 (3.20 h)	750	0.95	0.0004	1.02	0.0036	1.02	0.03	0.37	0.62	0.0026	0.0004	1.10	0.02	2.70	1.22	0.0025	0.0004
Ice Method #3 (5 min)	750	1.14	−0.0013	0.76	0.0074	1.06	0.14	1.55	7.05	0.0063	0.0028	1.42	0.16	3.52	2.12	0.0051	0.0023
Ice Method #3 (4.40 h)	750	1.11	−0.0041	0.78	0.0053	1.02	0.07	2.11	18.05	0.0044	0.0014	1.30	0.07	3.46	1.68	0.0039	0.0013
Ice Method #1 (10 min)	750					1.07	0.11	3.00	8.45	0.0035	0.0025	1.39	0.10	3.95	2.47	0.0031	0.0022
Ice Method #1 (4.50 h)	750	0.88	0.0036	0.87	0.0051	1.11	0.11	1.14	1.94	0.0011	0.0019	1.21	0.10	4.29	4.29	0.0011	0.0019

reflectance unit per degree of phase angle. The normalized parameters are defined as follows:

$$A' = \frac{B'_0}{B_1}, \quad \text{HWHM}' = \frac{(B'_0 - B_1)}{2(|a_1| - A_1)} \quad \text{and} \quad S' = -\frac{A_1}{B_1} \quad (9)$$

Another method to fit phase curves is the logarithmic model of Bobrov (1970),

$$r_{\log}(\alpha) = a_0 + a_1 \cdot \ln(\alpha) \quad (10)$$

which we fitted for $\alpha < 40^\circ$.

The B_0 from the linear model is replaced by $B'_0 = a_0 + a_1 \cdot \ln(10^{-3})$, where the value of 10^{-3} deg is the smallest phase angle considered to be reached by laboratory experiment. For more explanations and previous applications we refer to the work of Déau et al. (2013) and references therein. A complete table of morphology parameters for our experimental work can be found in Table 5.

Further, we applied an approximating function, as previously used by Rosenbush et al. (2002), to our data at phase angles from 0.5° to 60° (we exclude the point at $\alpha = 0^\circ$ from the fitting, since its value is systematically underestimated, see Section 2.4). This four-parameter exponential-linear function is defined as

$$I_{\text{fit}}(\alpha) = I_s \cdot \exp\left(-\frac{\alpha}{1.45 \cdot \text{HWHM}_B}\right) + I_b + \beta\alpha \quad (11)$$

where I_s is the amplitude of the opposition peak, I_b is the background intensity, β is the slope of the linear part, and HWHM_B is the half-width at half-maximum of the opposition peak. The enhancement factor ζ is defined as

$$\zeta = \frac{I_s + I_b}{I_b} \quad (12)$$

The parameters deduced from the application of this model can be found in Table 6.

2.4. Effects of finite angular resolution

In the literature, the opposition peak is generally described mathematically by its amplitude (B_0) and its angular half-width at half-maximum (HWHM; h) (e.g. Lumme and Irvine, 1976; Kaasalainen et al., 2001). In Hapke's terminology HWHM is $2 * h_s$ in the case of SHOE (Hapke, 1986, 2002). The amplitude of the peak is the ratio between the maximum of reflectance at near-zero

geometry and an extrapolated point at $\alpha = 0^\circ$ corresponding to a hypothetical phase curve without any opposition surge.

The optical resolution of a radio-goniometer is rarely a concern when measuring the reflectance of samples at moderate or high phase angles, as the phase curves are usually very smooth. The region of the opposition peak is an exception as the reflectance can vary abruptly within in the few degrees around the exact opposition.

For this reason, instruments designed specifically to study the opposition effects are optimized to achieve a very high angular resolution, by using detectors and light source placed at the end of very long arms. For example, the JPL long arm goniometer (Nelson et al., 2000) has an angular resolution: $\alpha = 0.05^\circ$, while the setup of Psarev et al. (2007) reaches an angular resolution of $\alpha = 0.005^\circ$. The maximum angular resolution of PHIRE-2 is: $\alpha = 0.5^\circ$. This is not sufficient to resolve fully the sharp opposition peaks seen in some materials and therefore the influence of the limited angular resolution of our measurements must be discussed in detail before analyzing the phase curves measured at low phase angles.

In this section we estimate quantitatively the effects of the limited angular resolution by extracting geometrical parameters from analytical opposition peak curves that we bin to simulate the decrease of resolution (peak rounding). A very similar discussion can be found in Kaasalainen et al. (2005). First, we calculated three different bidirectional phase curves from a set of Hapke parameters, chosen to represent a typical phase curve of a bright fine grained-medium. The following parameters are kept constant: $\omega_0 = 0.99$, $b = 0.27$, $c = -0.47$, $\Theta = 12^\circ$, $B_{0s} = 0.6$, $h_s = 0.1$, $B_{0c} = 1.0$, while for the parameter h_c one of the three values: 0.005 (narrow peak), 0.025 (intermediate) and 0.05 (broad) are chosen. ω_0 is the single scattering albedo, b and c the parameters of the two-term Henyey–Greenstein function and Θ is the macroscopic roughness slope angle. B_0 and h are the amplitude and width of the opposition peak, respectively, and the indices c and s refer to the physical mechanism involved in the opposition effect, coherent backscattering (c) or shadow hiding (s), respectively.

The three curves were first generated with a sampling of 0.1° . We then binned these curves with a bin size of 0.5° in order to simulate the resolution achieved on our instrument, and compared them to the original curves. The amplitude, defined as the ratio between the values of reflectance at the maximum of the opposition peak and the one at a hypothetical point at $\alpha = 0^\circ$ extrapolated from the linear part of the phase curve, was reduced by 19% for the narrow peak curve (Fig. 4a), by 5% for the intermediate (Fig. 4b) and by 2.5% for the broad peak curve (Fig. 4c). The HWHM of the opposition peak was reduced by 65% for the narrow peak, by 16% for the moderate and by 7.5% for the broad peak. The HWHM parameter is thus not usable for accurately estimating the width of the opposition peak on our data. Therefore, we use another criterion to estimate the width of the peak, similar to the HWHM but using the value of reflectance at $\alpha = 0.5^\circ$ instead of the value at $\alpha = 0^\circ$. This criterion (called w in the rest of the manuscript) varies linearly with the HWHM and is only marginally affected by the limited resolution (maximum variation of 5% in the case of the narrow peak). It can thus be used for reliable analyses of the peak width. The integrated area of the opposition peak (calculated for phase angle: $\alpha < 5^\circ$) differs only by 11%, 1.5% and 0.15% for the narrow, intermediate and broad peak, respectively, which makes the albedo calculations reliable in most cases.

2.5. Sample materials and sample preparations

A summary of the properties of the sample material used in this work can be found in Table 3.

Table 6

Fitted model parameters of selected datasets. The corresponding definitions can be found in Section 2.3.3.

Sample	λ (nm)	Rosenbush model parameters		
		ζ	HWHM	β
Aluminum oxide (flat)	650	1.21	1.29	0.0027
Aluminum oxide (rough)	650	1.16	1.74	0.0051
Salt <80 μm	650	1.06	0.55	0.0019
Salt 80–200 μm	650	1.10	0.45	0.0019
Spherglass 7010 (rough)	750	1.18	1.57	0.0037
Spherglass 5000 (rough)	750	1.19	4.04	0.0039
Spherglass 7025 (rough)	750	1.31	9.44	0.0022
Spherglass 5000 (flat)	750	1.21	5.17	0.0038
Glass bubbles	650	1.22	1.33	0.0043
Ice Method #2 (10 min)	650	1.21	0.33	0.0036
Ice Method #2 (3.20 h)	750	1.51	0.18	0.0021
Ice Method #3 (5 min)	750	1.10	0.97	0.0066
Ice Method #3 (4.40 h)	750	1.04	0.84	0.0044
Ice Method #1 (10 min)	750	1.13	1.20	0.0033
Ice Method #1 (4.50 h)	750	1.06	3.62	0.0011

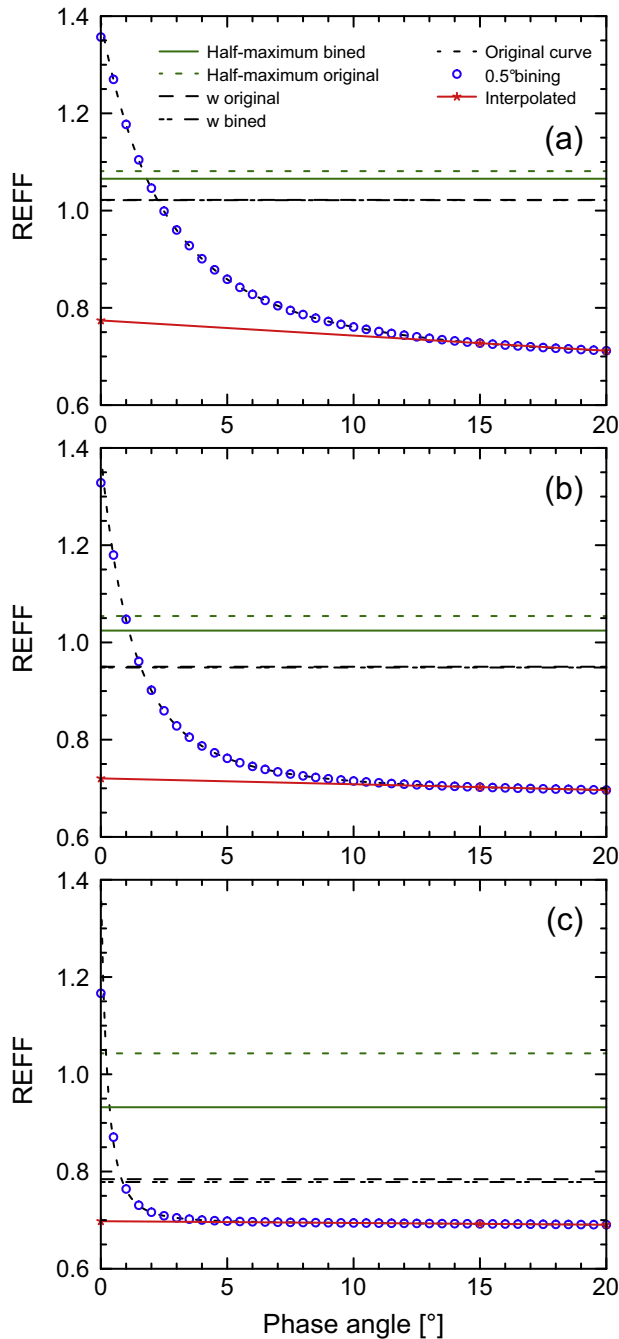


Fig. 4. Simulation of binning effects on the shape and amplitude of the opposition peak. Three phase curves with different angular widths of the opposition peak (broad to narrow, a to c) are generated with a 0.1° sampling in phase angle (black dashed lines) and binned to 0.5° (blue circles). The red point at $\alpha = 0^\circ$ is an interpolation of the shape of the phase curve out of the opposition peak. The green lines indicate the half-maximum of $\text{REFF}(\alpha = 0^\circ)$ with respect to the interpolated point and the green dotted lines the same values for the original curves. The vertical separation between these two lines is therefore a direct indication of the effect of binning. The horizontal black lines show similar quantities but defined relative to the REFF at $\alpha = 0.5^\circ$ rather than at $\alpha = 0^\circ$. This criterion, w , is far less sensitive to the binning effects. The effects of binning are more pronounced for narrow a peak (c) than for a broad peak (a). (For interpretation of the references to color in this figure legend, the reader is referred to the web version of this article.)

2.5.1. Production of micrometer-sized ice particles

Spraying liquid water into liquid nitrogen to produce small spherical particles of water ice is a procedure that has frequently been used to prepare the water ice fraction of cometary matter in previous laboratory simulations (Benkhoff et al., 1995; Sears

et al., 1999). In our previous work (Jost et al., 2013) we also used this technique to produce μm -sized particles of pure water ice using the setup built by Gundlach et al. (2011), for which detailed descriptions of the produced material are available. The main limitation of this setup is the production rate of fine-grained water ice, which is relatively low (2 g/h). We thus decided to build a new setup based on a similar principle but designed for a much higher production rate of water ice (a few tens of g/h).

The SPIPA (Setup for the Production of Icy Planetary analogs) employs an ultrasonic nebulizer originally built for veterinary use (Hippomed AIR ONE), which produces water droplets with a diameter in the range of $0.47\text{--}6\text{ }\mu\text{m}$ (as specified by the manufacturer). Contrary to the nebulizer spray used by Gundlach et al. (2011), the nebula produced by ultrasound is not pushed by a compressor and only flows by gravity. It is thus not possible to lead it directly into liquid nitrogen and a different setup had to be designed to freeze the liquid droplets quickly and keep them stored at low temperature. The nebula is conducted through a plastic tube inside a modified chest freezer with an interior temperature of about -60°C , cooled with a vessel containing liquid nitrogen. This low temperature limits the thermal metamorphism of the ice.

Currently, the SPIPA setup can produce about 50 g of water ice per hour, allowing us to produce enough ice to prepare large samples for PHIRE-2 in less than 1 h.

2.5.2. Size characterization of the micrometer-sized ice particles

The particles are almost perfectly spherical with smooth surfaces when observed under the SEM. The uppermost layer of particles of the sample shows evidence of frost deposition (see Fig. 5a) whereas the layers underneath are free of frost. The visible frost deposition almost certainly occurred during the brief transfer of the sample through the ambient air into the evacuated SEM.

A particle size estimation of the fresh ice particles from SEM images resulted in a mean diameter of $4.54\text{ }\mu\text{m}$ (standard deviation = $2.54\text{ }\mu\text{m}$) when regarding the number distribution of particle diameters. The size distribution is log-normal shaped. The volume moment mean (i.e. the mean of the mass distribution), often called $D(4, 3)$ or De Brouckere mean diameter (Allen, 1997) is $9.45\text{ }\mu\text{m}$. The mean diameter in this work ($d = 4.54\text{ }\mu\text{m}$) is by 50% higher than in the previous study (Gundlach et al., 2011; $d = 2.94\text{ }\mu\text{m}$) and the size distribution is broader.

2.5.3. Preparation of ice samples

Once the ice has been produced in the SPIPA setup, it must be introduced into one of the PHIRE-2 sample holders for photometric characterization. Three different preparation methods were used for this work.

2.5.3.1. Method #1. Method #1 consists of introducing liquid nitrogen into the steel vessel containing the ice particles to create a suspension. By stirring the suspension with a scoop, one prevents the formation of bigger agglomerates. As the liquid nitrogen evaporates the viscosity of the suspension increases and reaches a mud-like consistence. This suspension is then poured into a sample holder previously cooled in a bath of liquid nitrogen. The boiling nitrogen in the sample holder evaporates within some minutes until a flat ice surface remains, punctuated by some pits and cracks (see Fig. 6a).

The particles produced by this method keep a spherical shape overall, but have some angular surface irregularities (Fig. 5b). This may be a consequence of particle collisions during stirring of the suspension.

2.5.3.2. Method #2. Method #2 (see Fig. 6b) consists of depositing the frozen nebula directly onto a cold aluminum plate in contact

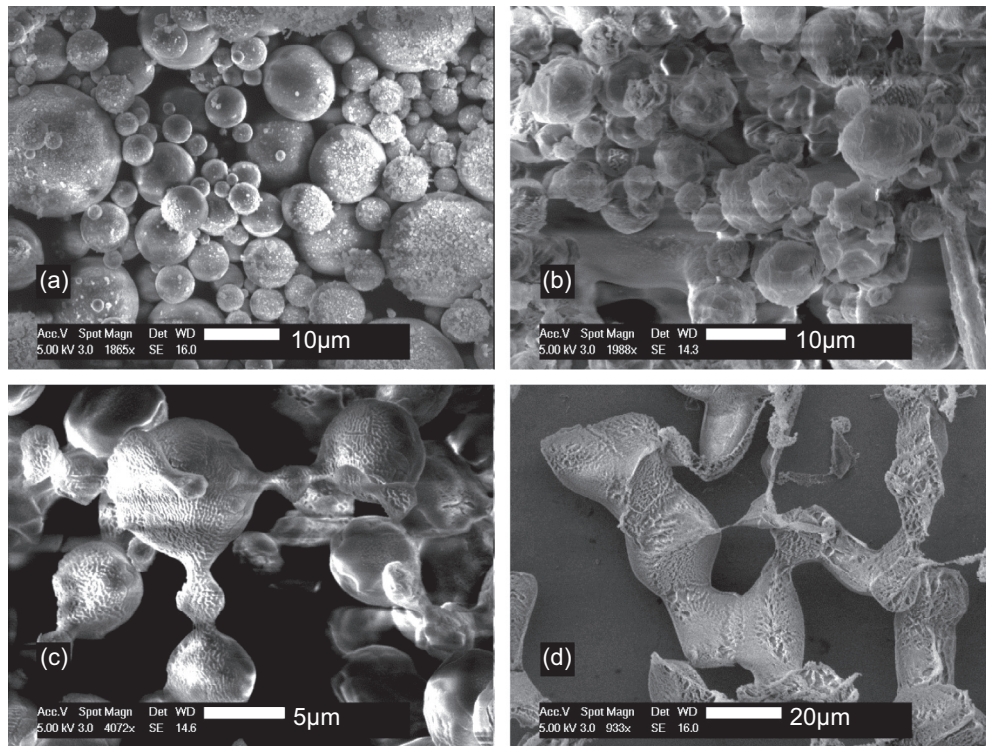


Fig. 5. Scanning-electron-microscope micrographs of water ice particles. (a) Fresh sample produced by Method #2 (direct spraying on a cold plate). The particles of the uppermost layer show some frost condensation (white chips on the surface of the spherical ice particles). The shape of the particles is almost perfectly spherical. (b) Fresh sample produced by Method #1 (suspension within liquid nitrogen), the shape looks more irregular, most probably through abrasion during the mixing within liquid nitrogen, where the suspension was constantly stirred up with a spatula. (c) Sample produced by Method #2 and left at $-30\text{ }^{\circ}\text{C}$ in a chest freezer for 1 h. The formation of bonds with neck regions between individual particles is visible. (d) The same preparation as in (c), but stored for 17 h. The original particles are still recognizable, but are completely irregular and grown together. There are no more particles left with diameters smaller than $10\text{ }\mu\text{m}$ and the bulk porosity increased compared to the fresh state.

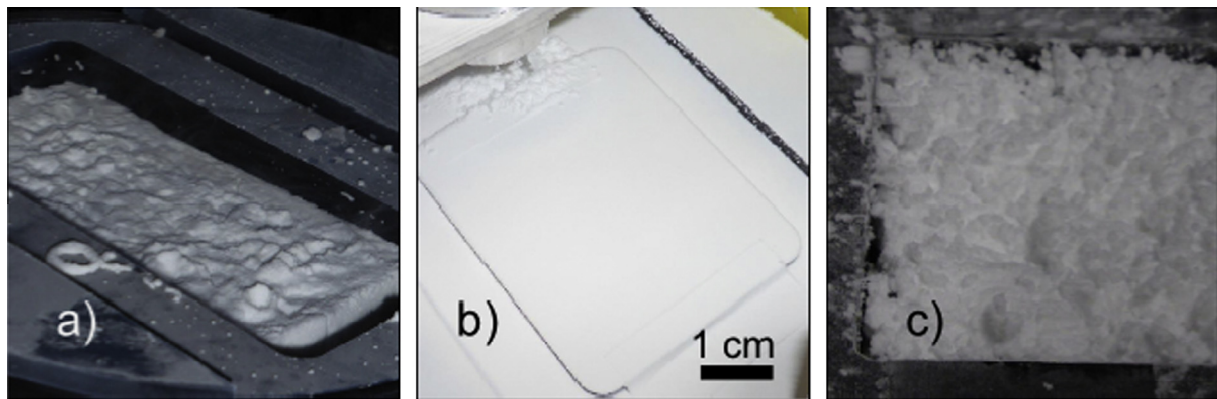


Fig. 6. Three different methods of surface preparation for fine-grained ice particles. (a) A suspension of the ice particles and liquid nitrogen is evaporated until only the ice remains (Method #1). (b) The frozen nebula is sprayed onto an aluminum plate (Method #2). (c) Preparation with a spatula (Method #3). See Section 2.5.3 for additional details on the preparation procedures.

with the liquid-nitrogen-cooled copper plate under it, producing a smooth and homogeneous surface made of ice spheres.

2.5.3.3. Method #3. Method #3 (Fig. 6c) consists of producing the ice in a stainless steel bowl and then transferring and flattening the material into the sample holder with a big spatula (also cooled by liquid nitrogen). This leads to a rough surface showing mm-sized agglomerates of finer ice particles.

3. Results

We investigated the morphological changes of fine-grained ice particles using SEM-micrographs. These structural evolutions with

time are strongly linked to the photometry observed with the same sample material. Further, we measured the bidirectional reflectance properties of different high-albedo icy analogs to investigate the effects of grain size distribution, particle shape and macroscopic surface roughness.

3.1. Morphological changes due to sintering effects

In Jost et al. (2013) we assigned observed temporal changes in photometric properties of micrometer-sized ice particles to sintering effects. Sintering of water-ice particles is the morphological change of the material driven by the tending toward decreasing the surface energy of the system. Material from the bulk of the

particles is transported to the neck regions, i.e. the region where particles are in or near contact. The neck radius grows with time, i.e. the curvature and surface area decrease. The growth rate is highly dependent on temperature. In our case (-30°C , atmospheric pressure), sublimation and recondensation of the material is the dominant physical process in mass transport (see Blackford, 2007 and references therein). At lower temperature and pressure, surface diffusion would be dominant.

Inside the cryo-SEM we tried to find evidence for in-situ evolution of the sample for about 30 min but could not observe any, most probably due to the low temperature (-140°C), which slowed down the metamorphism processes. It is not clear whether the platinum coating has some influence as well. When imaging in the cryo-SEM a sample which had previously been stored for 1 h in a chest freezer at -30°C after production, we clearly see necks and junctions between particles (Fig. 5c), while the surface structure is ribbed compared to the original material (Fig. 5a). This change in surface texture is either a consequence of the particle sublimation, or an evolution of the structure of the frost deposited at the surface of the particles. The sample's texture after 17 h of storage inside the freezer (Fig. 5d) is very different from the original one. All particles smaller than about $10\text{ }\mu\text{m}$ have totally vanished, while bigger particles have merged into a lattice-like structure with large neck regions and some filigree junctions formed or remaining between more distant particles. It is possible that the junctions are leftovers of sublimated particles and bonds. In general the particles' surface texture is rougher than after 1 h (Fig. 5c) and shows a honeycomb-like structure in some areas. It seems very likely that the material of the vanished small particles sublimed and, at least to some extent, recondensed onto the bigger particles. When comparing Fig. 5d to a and b, it seems that not only the shape changed with time, but also the bulk porosity increased by sublimation.

This series of SEM images supports the assumption of Jost et al. (2013) that a morphological change of the ice particles from almost perfect spheres toward more complex structures with contact surfaces, irregular shapes, neck regions and junctions is the driver of the observed temporal photometric behavior. As smaller particles disappear, the average size of scattering units grows with time. In addition, the surfaces of individual particles seem to evolve from smooth to rough at sub-micrometer scale.

3.2. Photometric measurements of non-volatile materials

3.2.1. Sodium chloride

Two agglomerate size fractions of crushed sodium chloride were measured, in order to study the influence of particle size on the reflectance in the case of irregularly shaped grains. Both samples show a very isotropic scattering behavior. The coarser fraction ($80\text{--}200\text{ }\mu\text{m}$) is 5–10% brighter than the finer fraction ($<80\text{ }\mu\text{m}$) in all geometries but the shapes of their phase functions are nearly identical (Fig. 7). In particular, we do not observe significant differences in the amplitude and the angular width of the opposition peaks.

3.2.2. Aluminum oxide abrasive

Measurements with aluminum oxide abrasive powders demonstrate the strong influence of macroscopic surface roughness on the sample phase function. The flat surface is associated with a narrower opposition peak and a less steep phase curve at non-opposition geometries, than the rough surface (Fig. 8). The total integral of the curve at normal incidence, $i = 0^{\circ}$, differs only by 1.5% between the two surfaces whereas the integral of the opposition peak is 35% higher for the flat sample. The amplitude of the peak is 60% higher in the case of the flat surface. For high incidence angles, $i = 60\text{--}70^{\circ}$, the rough surfaces shows a more

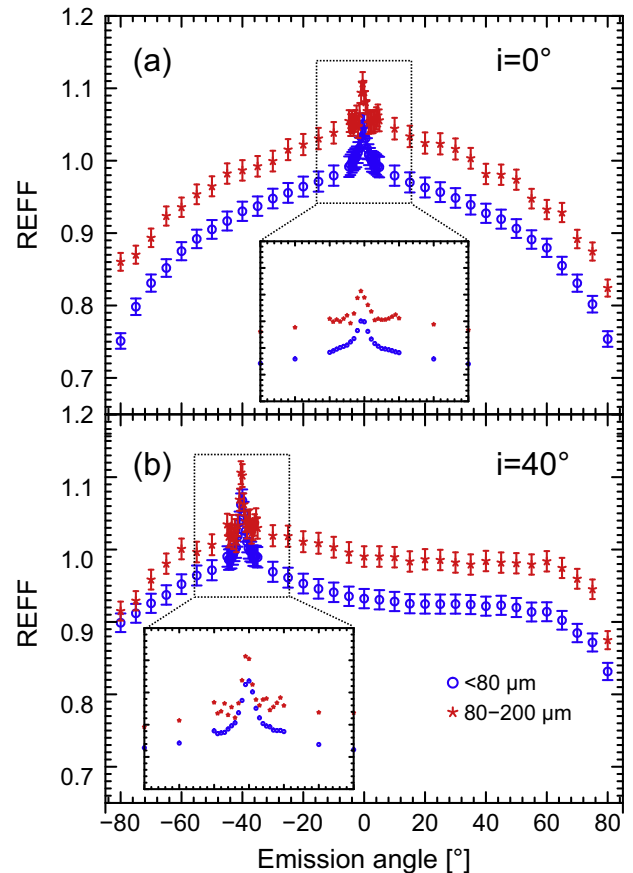


Fig. 7. Phase curves at (a) $i = 0^{\circ}$ and (b) $i = 40^{\circ}$ of sodium chloride crushed with a mortar and sieved to two different particle size fractions. The irregular particle shapes, are very similar for both size fractions. The phase curves are nearly identical, the surface prepared with the smaller particles being darker by about 10%. The amplitude and width of the opposition peak do not show major differences.

pronounced backscattering whereas scattering at large phase angles is almost absent. Significant forward scattering at phase angles higher than 100° is observed for the smooth surface. We compared these two curves with a dataset published by Nelson et al. (2000). The measurements reported in Nelson et al. (2000) were acquired with slightly smaller particles ($1\text{ }\mu\text{m}$) and a better angular resolution using the JPL long arm goniometer. Normalizing the reflectance values for $\alpha = 5^{\circ}$, we get a very good agreement with our data, especially for the rough surface, down to $\alpha = 0.5^{\circ}$ (Fig. 9). We underestimate the value of reflectance at 0° because of the limited angular resolution of the PHIRE-2 instrument as discussed in Section 2.4.

3.2.3. Spheriglass

A series of commercially distributed fine-grained soda-lime glass spheres (Potter Industries Spheriglass) shows the effect of different particle-size ranges and their mixture on the phase function. Spheriglass 5000 was also used by Hapke et al. (2009) for measurement on two different instruments and thus acts as a good comparison of hardware capabilities. The raw (mixed) material (5000) is compared to its small (7010) and big (7025) fractions in Fig. 10. All three surfaces were prepared with a similar degree of roughness (sprinkled with a sieve). At moderate incidence angles ($5\text{--}20^{\circ}$) the general shape is very similar for all types, but the opposition region shows differences. The small fraction has a slightly broader peak but a less steep slope between $e = -15^{\circ}$ and $e = -5^{\circ}$. Type 7010 is less reflective in the forward direction at phase angles larger than 100° than bigger particles. Type 7025

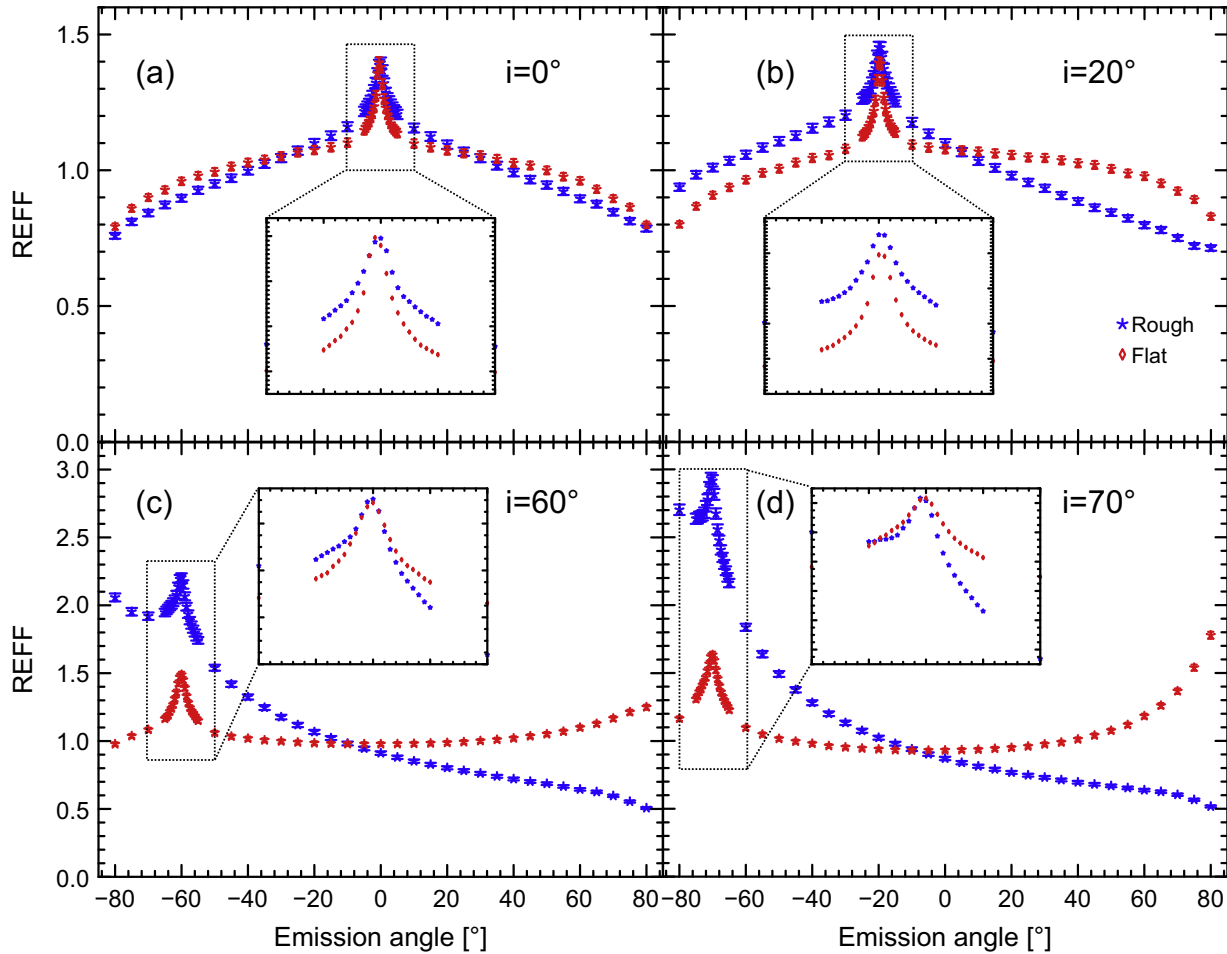


Fig. 8. Phase curves measured for two different surfaces prepared with aluminum oxide abrasive (Microgrit WCA 1, $\sim 2 \mu\text{m}$) at four different incidence angles: (a) $i=0^\circ$, (b) $i=20^\circ$, (c) $i=60^\circ$, (d) $i=70^\circ$. The two surfaces were produced with different surface preparation methods to investigate the effects of macroscopic roughness. The “flat” surface was slightly compacted and flattened with a Teflon cube. Later, some material was sprinkled onto this flat surface with a sieve to produce the “rough” surface and its reflectance was re-measured. The rough surface shows a broader and lower opposition peak at $i=0^\circ$. At high incidence angles ($i=60^\circ$, 70°), it shows a much higher backscattering and no scattering in the forward direction. Similar effects of the surface preparation method in the case of martian analogs were documented by [Pommerol et al. \(2013\)](#). The blue curve in the zoom box is vertically shifted by -0.7 (c) and -1.3 (d). (For interpretation of the references to color in this figure legend, the reader is referred to the web version of this article.)

shows a feature with a local maximum at $\alpha = 2\text{--}5^\circ$, that we attribute to a solid-state glory effect (see discussion in Section 4.2).

We show in [Fig. 11](#) the roughness effects for glass type 5000, which appear smaller than the ones observed for aluminum oxide ([Fig. 8](#)). There is almost no difference between the reflectance curves of both surfaces measured at normal incidence ($i=0^\circ$), whereas for an incidence of $i=60^\circ$, the backscattering is reduced by about 20% and scattering at large phase angles increased by about 30% for the flat sample. A comparison of these datasets with the ones of [Hapke et al. \(2009\)](#) measured on the JPL long arm goniometer and Bloomsburg University Goniometer (BUG) in the same figure shows considerable discrepancies at $i=0^\circ$ ([Fig. 11](#)). This is very surprising as an excellent agreement between measurements of similar samples performed on the BUG and PHIRE-2 instruments was reported by [Pommerol et al. \(2013\)](#) and demonstrated again here with measurements on aluminum oxide samples ([Fig. 8](#)). An excellent agreement is also demonstrated by [Hapke et al. \(2009\)](#) between the measurements with the JPL and BUG instrument, excluding measurement or calibration error as the source of the discrepancy. Therefore, we are left with the hypothesis that the material measured by [Hapke et al. \(2009\)](#) and the material that we measured must be significantly different, despite the similar denominations by the provider.

3.2.4. Comparison with results from [Shkuratov et al. \(2002\)](#)

The most systematic experimental survey of planetary analogs in the past was performed by [Shkuratov et al. \(2002\)](#). The authors investigated effects of albedo, bulk compression, particle size, wavelength and particle shape on the opposition effect and degree of polarization. While their setup can measure polarization and has a very high angular resolution, it is restricted to phase angles of $0.2\text{--}4^\circ$ and two spectral bandpasses (450 nm, 630 nm). The PHIRE-2 instrument has a lower angular resolution but can reach phase angles up to 150° . It has a bandwidth between 450 nm and 1064 nm. Furthermore the selection of sample materials was different. These differences make a direct quantitative comparison of their findings with our results very difficult. The only similar sample was aluminum oxide abrasive. In a qualitative way, their results of compressed and uncompressed aluminum oxide particles are consistent with our findings of flat and sprinkled aluminum oxide samples. Their way of compressing samples with a glass plate has a similar effect as when we flattened our sample with a spatula, the surface relief is smoothed and the uppermost particle layers are compacted. Both procedures result in a higher and narrower opposition peak ([Fig. 8](#)).

The findings by [Shkuratov et al. \(2002\)](#), that a high albedo increases the amplitude of the opposition peak, has no direct

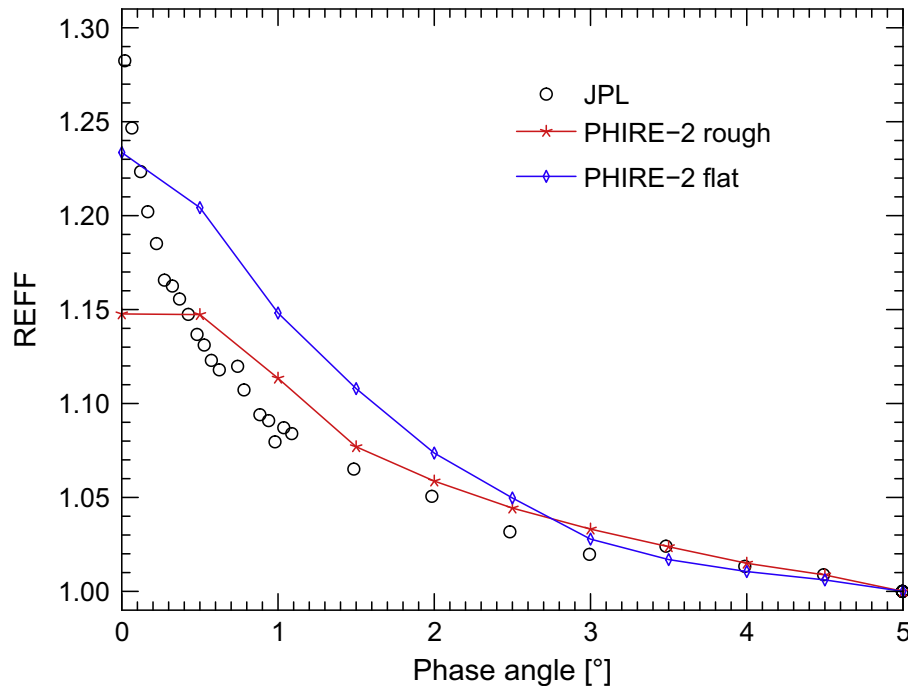


Fig. 9. Comparison of PHIRE-2 reflectance data ($i = 0^\circ$, $\lambda = 750$ nm) with data published for a similar sample by Nelson et al. (2000). The sample is in our case aluminum oxide abrasive (Microgrit WCA 1) with 50% of particles within 1.77–2.25 μm (same as Fig. 8). JPL data were acquired with 1 μm particles. All curves are normalized to $\alpha = 5^\circ$. The coincidence is very high at $\alpha > 0.5^\circ$, whereas binning effects as described in Section 2.4 reduce the amplitude of the peak at 0° . The surface preparation is not specified in Nelson et al. (2000), but we observe a better agreement with our rough surface than with our flat surface.

influence on our work since we restricted our choice of sample material only to albedos close to unity. A direct comparison of particle shape effects with our glass spheres and hollow bubbles would not be appropriate because the size and distribution are not comparable.

3.3. Measurements of fine-grained ice particles

As in our previous work (Jost et al., 2013), we measured time series of the reflectance curves of the icy samples to observe the photometric effects of the strong morphological changes within the sample material caused by its metamorphism. In general, a decrease of reflectivity at phase angles smaller than 20° is observed and in some cases, an increase of reflectivity at large phase angles.

Whereas only one preparation method was used in the previous work, we compare here results obtained with the three different surface preparation methods described in detail in Section 2.5.3.

In Fig. 12, the temporal evolution over 22 h of the reflectance of the “Method #1” sample is shown for a fixed incidence angle: $i = 20^\circ$ and a single wavelength: $\lambda = 750$ nm. The reflectance at opposition ($e = -20^\circ$) and at moderate phase angles decreases with time, while at larger phase angles ($\alpha > 50^\circ$) the reflectance only increases between the first two measurements and then keeps an almost constant value.

Fig. 13a shows similar data as Fig. 12 but for the “Method #3” sample and zooming in the region of the opposition peak. One can observe that the overall reflectance in this range of phase angles is decreasing with time (by about 7% in 5 h), and that the amplitude of the opposition peak [$\text{REFF}(\alpha = 0^\circ) - \text{REFF}(\alpha = 10^\circ)$] is decreasing even faster. The width of the opposition peak decreases by about 1° in 5 h. The first sequence (0.05 h) of Fig. 13a is shown in Fig. 13b at different wavelengths. The reflectance measured at 1064 nm is systematically lower than at other wavelengths because of the absorption by H_2O at 1.1 μm . The height of the opposition peak continuously increases with

wavelength, the peak amplitude at 1064 nm being higher by 60% than at 550 nm. The angular width also depends upon wavelength in a similar way. Whereas at shorter wavelengths there is a clear change in slope around $\alpha = 2^\circ$, the shape of the peak becomes more linear toward NIR.

We compiled phase curves for all three preparation methods of ice samples (as well as the three samples from the previous work for $i = 60^\circ$) in Fig. 14 to analyze the effects of surface preparation and their temporal evolutions. At $i = 20^\circ$ (Fig. 14a), the sample with the highest roughness (Method #3) is the brightest around opposition and at phase angles smaller than 30° . The two other surfaces have a very similar reflectance at phase angles smaller than 60° whereas Method #1 (prepared in liquid nitrogen) shows a higher reflectance at $e > 40^\circ$. All samples show a decrease in reflectance of about 10–15% at low phase angles with time. The sample prepared with Method #2 shows an almost parallel shift in brightness, whereas the one prepared with Method #3 shows higher values of reflectance at $e < -35^\circ$. This is potentially an effect of the high roughness. Method #1 shows an opposite behavior: the sample scatters more light in the forward direction with time. This behavior was already observed for all three samples by Jost et al. (2013). There, the ice was also prepared in liquid nitrogen, but the bulk was crumbled and prepared with a spatula in a similar manner as Method #3. The scattering at large phase angles observed for the sample prepared with Method #1 could be interpreted by a lower roughness at microscopic scale, as the particles suspended into a liquid sediment to form a smooth desiccated crust. A similar behavior was observed by Pommerol et al. (2013) for martian analogs prepared with liquid water: the phase curves of samples prepared in such a way became more strongly forward scattering after the sample had dried out.

At $i = 60^\circ$ (Fig. 14b), we see good indications that high macroscopic roughness causes higher reflectivity at low phase angles, the sample prepared by spraying particles on a flat plate (Method #2) being the darkest at low phase angles. The samples of our

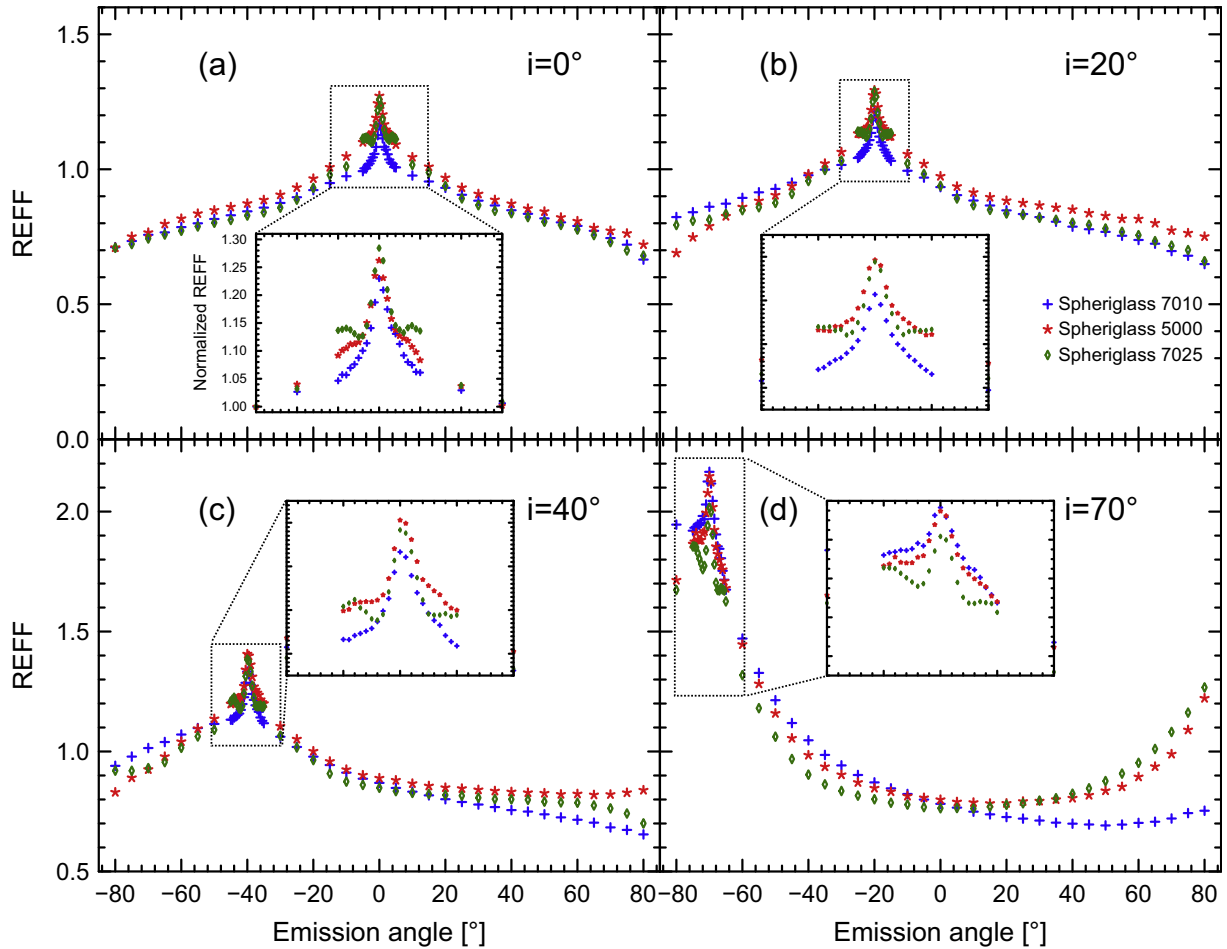


Fig. 10. Phase curves measured for three different particle size distributions of the Spheriglass particles: (a) $i = 0^\circ$, (b) $i = 20^\circ$, (c) $i = 40^\circ$, (d) $i = 70^\circ$. Type 5000 is the raw (unsorted) material (90% within 0.5–19.3 μm). Type 7010 is the finer subset (0.5–10.0 μm) and type 7025 the coarser subset (10.0–19.3 μm). The surface is prepared by sprinkling grains on a flat substrate with a sieve. The smaller grains show a slightly broader peak at $\alpha < 5^\circ$ while the slope at $5^\circ < \alpha < 20^\circ$ is less steep ($i = 0^\circ$) and the scattering in the forward direction is less pronounced ($i = 70^\circ$). The zoom box in (a) shows the opposition region normalized at $e = 15^\circ$. Type 7025 shows a local maximum at 3–5° resulting from glory. Type 5000 has no distinct peak due to broader particle size distribution, but is still brighter at these geometries than type 7010, which shows no glory feature.

previous work are all in-between Methods #2 and #3, which indicates a moderate roughness. The scattering at large phase angles observed for samples prepared with Method #1 is less pronounced than at $i = 20^\circ$, but all samples show an increase in reflectance at large phase angles, at least in a fresh state.

3.4. Hapke model parameters

In Table 4 we provide Hapke photometric model parameters for all sample materials used in this study. We did not use the anisotropic multiple scattering calculation since it does not improve the fitting accuracy significantly and differences in individual parameters lie inside the confidence intervals. As we only used bright materials (ice or ice analogs) the single scattering albedo ω_0 is equal or very close to 1 and well constrained. The mean slope angle parameter $\bar{\theta}$ is very low for most samples but not very well constrained in the upper limit. Nevertheless, it seems to follow real variations of sample roughness in the case of the aluminum oxide and Spheriglass 5000 samples. The reliability of the opposition peak parameters (B_s , h_s , B_c , h_c) is doubtful since the distinction between SHOE and CBOE is not trivial. We used both the CBOE and SHOE model for data fitting because SHOE alone (with a limitation of $B_s = 1$) could not reproduce the full amplitude of the opposition peak in some cases. It is shown again that single particle

phase functions can compensate for roughness effects. The two aluminum oxide samples should in theory have the exact same values since particle shape does not change when a rough surface is flattened, the same is valid for Spheriglass 5000.

The asymmetry parameter, g , is also deduced from b and c . For ice, g has values from -0.63 to -0.17 . The smoother the surface, the lower is g (Method #2 = $-0.54/-0.63$). By comparing these values to asymmetry factors of icy satellites like Enceladus ($g = -0.38$; Verbiscer et al., 2005) or Europa ($g = -0.15$; Verbiscer et al., 2005) no definitive conclusion about matching can be drawn, as our uncertainties are of the order of ± 0.1 . The numbers derived by fitting our experimental data, however differ significantly from the value of $g = +0.53$ for terrestrial snow (Verbiscer et al., 1990).

3.5. Morphology parameters

While we used the complete dataset for each sample (i.e. all incidence directions) to fit the Minnaert model (Table 5), the morphology parameters were only deduced from the curves measured at $i = 0^\circ$. It showed that the HWHM parameter is poorly constrained and a quantitative comparison is not appropriate. Samples with a flat surface show a slightly higher amplitude than the equivalents with a rougher surface. This is true for aluminum oxide and Spheriglass 5000. On ice samples it is only significant on the

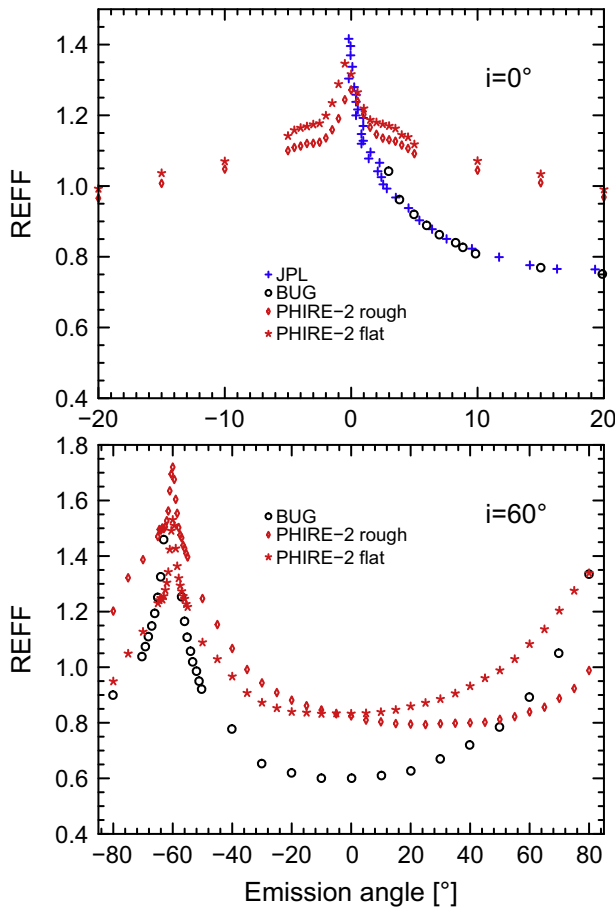


Fig. 11. Comparison of PHIRE-2 data (750 nm) measured with the Spheriglass 5000 samples with reflectance data acquired with other instruments (700 nm). Data of JPL-long arm-goniometer and Bloomsburg University Goniometer are from Hapke et al. (2009). The sample type in this publication is not clearly specified but we assumed Spheriglass 5000. At $i = 60^\circ$ our measurement shows an overall similar curvature as BUG in the case of a flat surface preparation but a 20% offset that we cannot assign. For vertical incidence, $i = 0^\circ$, there is absolutely no agreement with data from Hapke et al. (2009) except at opposition. The sample in this study and by Hapke et al. (2009) was probably different.

normalized amplitude. The slope of aluminum samples is increased by almost a factor of 2 for the rough surface, whereas there is no significant difference for the Spheriglass 5000 samples.

4. Discussion

After having measured the reflectance of different surfaces of ice and materials acting as ice analogs, we discuss in this section the relationships between the morphological properties of the samples and their bidirectional reflectance properties.

4.1. The opposition effect on icy surfaces

When interpreting the opposition effect on icy surfaces, several parameters that influence this effect have to be kept in mind. Beside quantities like particle shape, macroscopic roughness and particle size, other quantities such as packing density, absorption and wavelength play a major role. The main factor that defines the scattering efficiency of a single particle is the size parameter, defined as $x = \pi D/\lambda$, the ratio between the particle size and the wavelength of the incoming light. In addition, the extinction coefficient (imaginary part of the refractive index) of the particle material is also likely to vary with wavelength. In the case of water ice, it

ranges from 2.3×10^{-3} (550 nm) to 1.9×10^{-6} (1064 nm) (Warren and Brandt, 2008), which is a difference of almost three orders of magnitude. Since there is an inverse correlation between the strength of coherent backscattering and the absorption (Wolf et al., 1988), darker materials should have a smaller CBOE. Another crucial parameter, the mean free path, is strongly influenced by the bulk porosity or packing density. The lower the packing density, the longer is the mean free path, which reduces coherent backscattering (see e.g. Mishchenko, 1992; Mishchenko et al., 2006; Muinonen et al., 2012).

This implies that the sample morphologically evolved after 17 h of sublimation (Fig. 5d), which has a higher porosity, and therefore a longer mean free path than in its original state, should display a reduced coherent backscattering compared to a fresh sample. This is consistent with results presented in Fig. 16, which show a reduction of the amplitude of the opposition effect itself in addition to a decrease of the reflectance at moderate phase angle. The dashed lines in Fig. 16a represent the change in REFF at $\alpha = 10^\circ$ for different wavelengths. The rate of change seems to be independent of wavelength, whereas the offset for the 1064 nm wavelength curve is caused by the 1.1 μm absorption band of H_2O . Solid lines in Fig. 16a represent the change in reflectance at the opposition geometry. Again, the rate of decrease in the reflectance seems to be independent of wavelength. The decrease rate for $\alpha = 10^\circ$ is marginally lower which indicates a decrease of the opposition peak amplitude with time. This becomes more obvious when analyzing the difference between opposition and non-opposition geometry, as plotted in Fig. 16b. The brightnesses in different filter bands show that the amplitude is increasing with wavelength, except at 1064 nm where it is slightly lower. The decrease rate is identical for all wavelengths and represented by a linear fit (dashed lines). A dependence of CBOE on wavelength was proposed and observed by different authors (e.g. Van Albada et al., 1990; Mishchenko, 1992; Hapke et al., 1998; Hapke, 2002). Both peak properties, amplitude and width, should positively correlate with wavelength when the grain size is larger than the wavelength.

The observation of a wavelength dependence of the opposition peak for fresh small-grained ice particles indicates that a significant fraction of the opposition effect can be attributed to coherent backscattering. Its decrease with time as the packing density decreases and the average particle size increases, is visible in Fig. 5. This means that the relative contribution of CBOE to the total opposition effect compared to the contribution of SHOE is decreasing with time. By contrast the change in particle morphology as spherical particles grow to more complex structures with more surface irregularities should induce an increase in coherent backscattering, as the light has more opportunities to be multiply scattered, as it scatters not only on entire particles but also on their irregularities. This leads to the conclusion that, in this case, the particle size has a stronger influence on the coherent backscattering than the microscopic surface irregularities.

It seems likely that we underestimated the influence of macroscopic roughness effects on icy surfaces in our previous work. We had tested if changes of roughness on a soda-lime-borosilicate glass bubble sample had visible effects on its phase curve and found no evidence for any. However, this particular sample shows very low cohesion between particles and thus behaves like a low-viscosity fluid. These particles do not form agglomerates, and roughness is therefore limited to a 1-particle-radius scale. On the other hand, the Spheriglass material or the ice spheres always form agglomerates, or large scale structures, similar to the “fairy castle” structures described by Hapke and van Horn (1963), which certainly contribute to shadow-hiding effects and thus strongly affect the phase curves. A complementary explanation for the shadow hiding effect is given by Penttilä (2013), who shows that quasi-specular reflection on a rough surface contributes to the opposition

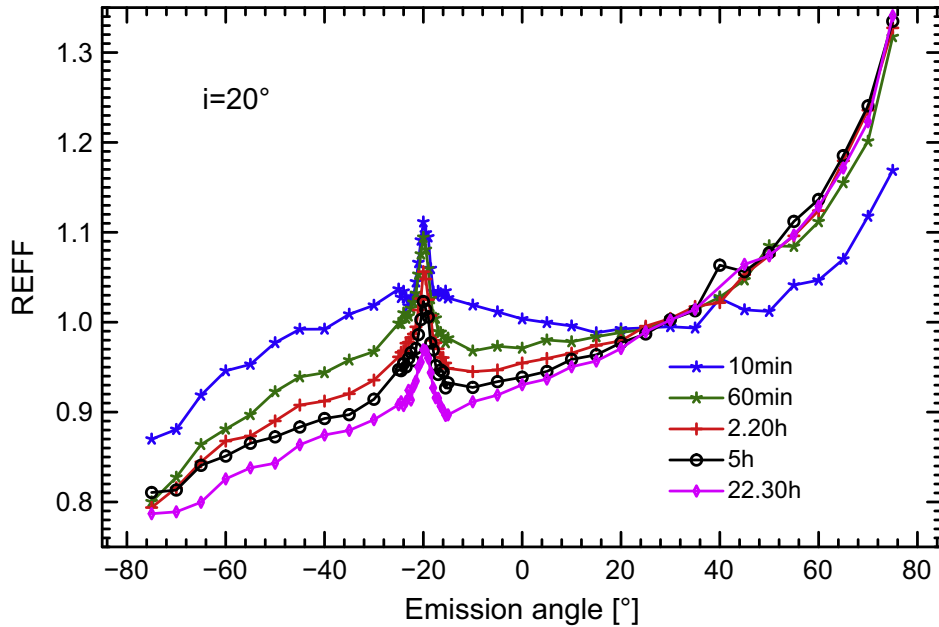


Fig. 12. Temporal evolution of the phase curves at incidence $i = 20^\circ$ measured on fine-grained ice particles prepared by evaporating a suspension with liquid nitrogen (Method #1). All measurements shown here were acquired at a wavelength of 750 nm. The reflectance at opposition ($e = -20^\circ$) and moderate phase angles decreases with time, while the forward fraction ($e > 25^\circ$) increases after the first measurement and then stays more or less constant.

peak as well as affecting the brightness at large phase angles. With increasing roughness more surface facets are tilted in a way that they reflect more light backward in the incidence direction, while this fraction is missing at large phase angles. This assumption is nicely illustrated by Figs. 8c, d and 14b.

The total reflectance value in the opposition geometry (opposition peak and linear background) of ice samples could in theory serve as a roughness indicator. As shown in Fig. 15 the maximum reflectance at zenith illumination and observation is correlated with macroscopic roughness. The sample prepared by Method #3 has the highest roughness and highest reflectance. The preparation with Method #2 results in the lowest macroscopic roughness and has a lower reflectance at opposition. The sample prepared by Method #1 shows a level of reflectance intermediate between the two others. This is consistent with the visual inspection reported in Fig. 6. The reflectance at opposition shows an exponential decrease with time for all three samples, which creates a non-unique relation between roughness and reflectance. It seems reasonable to assign the changes with time to the microscopic level, whereas the initial difference between the samples results from macroscopic scale differences. It is worth noticing that the resulting reflectance differences influenced by microscopic and macroscopic contributions are about of the same order of magnitude which makes it difficult to distinguish between them.

In addition to the differences in the asymmetry factor between micrometer-sized ice particles and terrestrial snow already highlighted in Section 3.4, it is worth noticing that contrary to terrestrial snow (see e.g. Shkuratov et al., 2002), for which the opposition effect is almost absent, our small-grained ice particles show a strong opposition peak. This is a fundamental photometric difference between two samples made of the same material. This leads to the conclusion that the microphysical state of water ice is strongly influencing its scattering properties and the observation of icy objects in the outer Solar System at low phase angle can bring valuable information about the structure of the grains at their surface.

4.2. The glory effect

For very fine-grained material (such as Spherglass 7010) with particles smaller than $10 \mu\text{m}$, the primary glory peak would lie at phase angles between 5° and 10° for visible light, but seems already too weak to observe, as stated by Laven (2005a). We do not clearly observe the glory effect in the phase curve for the unsorted Spherglass sample (type 5000) but the reflectance factor is higher in the range $\alpha = 2-5^\circ$ compared to type 7010 and the curvature is concave instead of convex (see Fig. 10a). We interpret this difference as a leftover of the glory, explained by the broader distribution of particle sizes, which causes a broadening of the peak (Mayer et al., 2004).

To confirm that the feature observed in the phase angle range $\alpha = 2-5^\circ$ with material type 7025 is indeed caused by glory, we have studied in more detail its dependence on wavelength. The phase curves measured through the six different bandpass filters are plotted in Fig. 17a and show the expected shift of the position of the peak with wavelength. The peaks' positions are then plotted as a function of wavelength in Fig. 17c. Simulations using Mie theory fit quite well with a mean diameter of $10 \mu\text{m}$ (normal distribution with $\sigma = 20\%$) as shown in Fig. 18. The height of the central peak compared to the local minima is plotted against the wavelength in Fig. 17b, whereas Fig. 17d shows the integral of the central peak as a function of wavelength (the area between the peak and a linear continuum between the two local minima, as indicated for $\lambda = 1064 \text{ nm}$ in Fig. 17a). Both the amplitude and the integral show a linear correlation with wavelength. To investigate whether wavelength dependencies occur only in the opposition region or as well at large phase angles, we measured the same sample with an incidence angle of 70° , for which phase angles of 150° are reached. It seems that for glass particles larger than the wavelength, there is no wavelength dependence for $\alpha > 10^\circ$.

The observation of glories on solid surfaces of small glass particles suggests that the same phenomenon might be expected with ice spheres in a similar size range. Obviously glories cannot occur

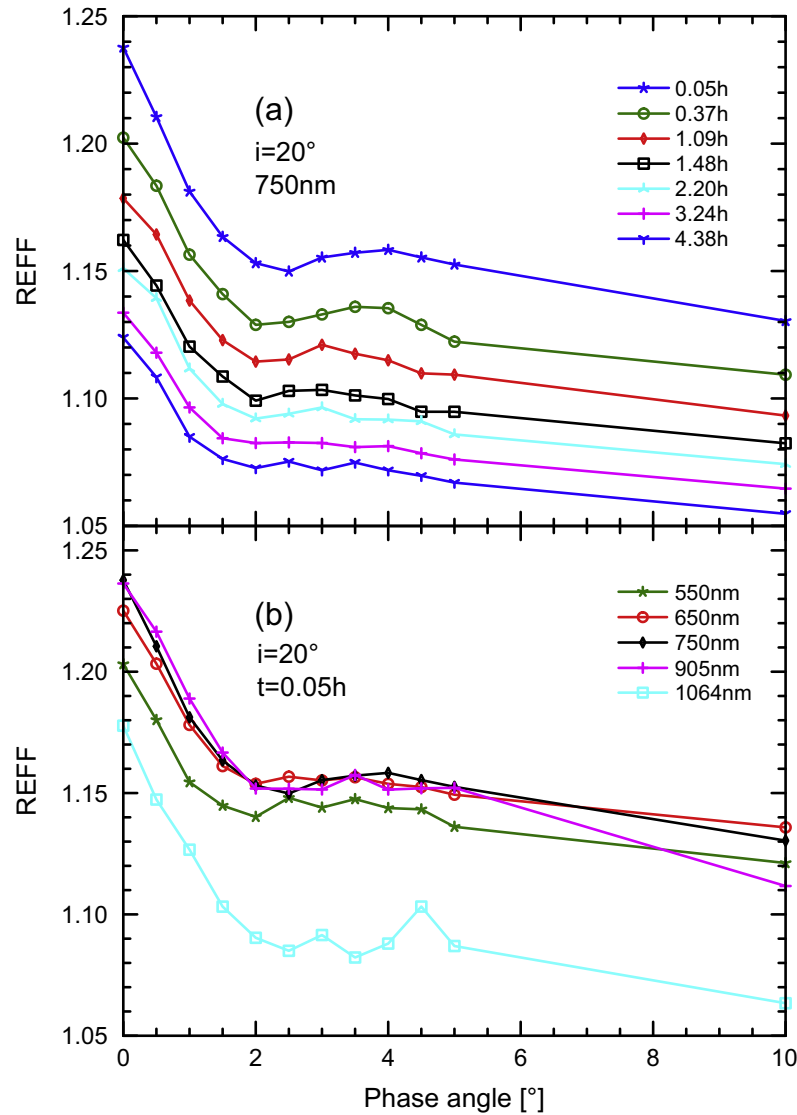


Fig. 13. (a) Temporal evolution of the opposition peak measured for ice prepared by Method #3 at $\lambda = 750$ nm and $i = 20^\circ$. A general decrease of reflectance is observed with time. The glory is clearly visible as a concave shape at $\alpha = 2\text{--}5^\circ$ at the beginning of the measurement sequence, but vanishes with time. (b) Reflectance curves of the 0.05 h sequence at different wavelengths. The material is significantly darker in the NIR, due to the absorption band of water at 1100 nm. The height and the width of the opposition peak are dependent on wavelength: the longer the wavelength, the higher and broader is the peak. This is a strong indication for Coherent Backscattering Opposition Effect, because Shadow Hiding Opposition Effect does not depend on wavelength.

on terrestrial ice and snow surfaces because particles are too large and flake-shaped instead of spherical.

Nevertheless we could observe weak glories on ice samples measured with PHIRE-2 with all preparation methods (see curves in Fig. 14). The most visible is in Fig. 13a, where the maxima are most pronounced as a concave shape in the phase angle $\alpha = 2\text{--}5^\circ$ at the beginning of the measurement sequence and disappear after a few hours. Furthermore, their relative strength is similar to Spherglass 5000 particles, which is consistent with the fact that wider particle size distributions broaden the glory. We repeated the experiment with preparation Method #3 to decrease time intervals between measurements by reducing incidence directions and filter numbers, in order to get a higher time resolution of 13 min. During 90 min we observed a slight shift of the angular position of the first maximum by about 1° , but the measurement uncertainty is not significantly smaller. This evolution may indicate an increase of the mean particle size.

As we could do statistics on hundreds of particles from SEM images, we have used these size distributions for Mie theory

simulations. The software used is MiePlot developed by Philip Laven, which can be downloaded from <http://www.philiplaven.com/mieplot.htm>.

The angular positions of the first glory maxima on the simulated phase curves are in good agreement with the measured locations (see Fig. 19). Although the particles prepared in liquid nitrogen show more angular shapes (see Fig. 5b), they are still able to produce glory of a similar order of magnitude as the perfectly spherical particles. It is possible that the shape changes back to more roundish after a certain time by sublimation/recondensation processes. The fact that the simulation performed with the size distribution derived for a sample after 1 h of metamorphism, creates a more pronounced glory than with the size distribution of the fresh sample might be a bias caused by the method used to determine the size distribution. Indeed only the relatively spherical particles were counted whereas the irregular bonds between particles, which should not create any glory, were ignored.

Another possibility to explain the disappearance of the glory effect on ice with time is the increase of surface irregularities as

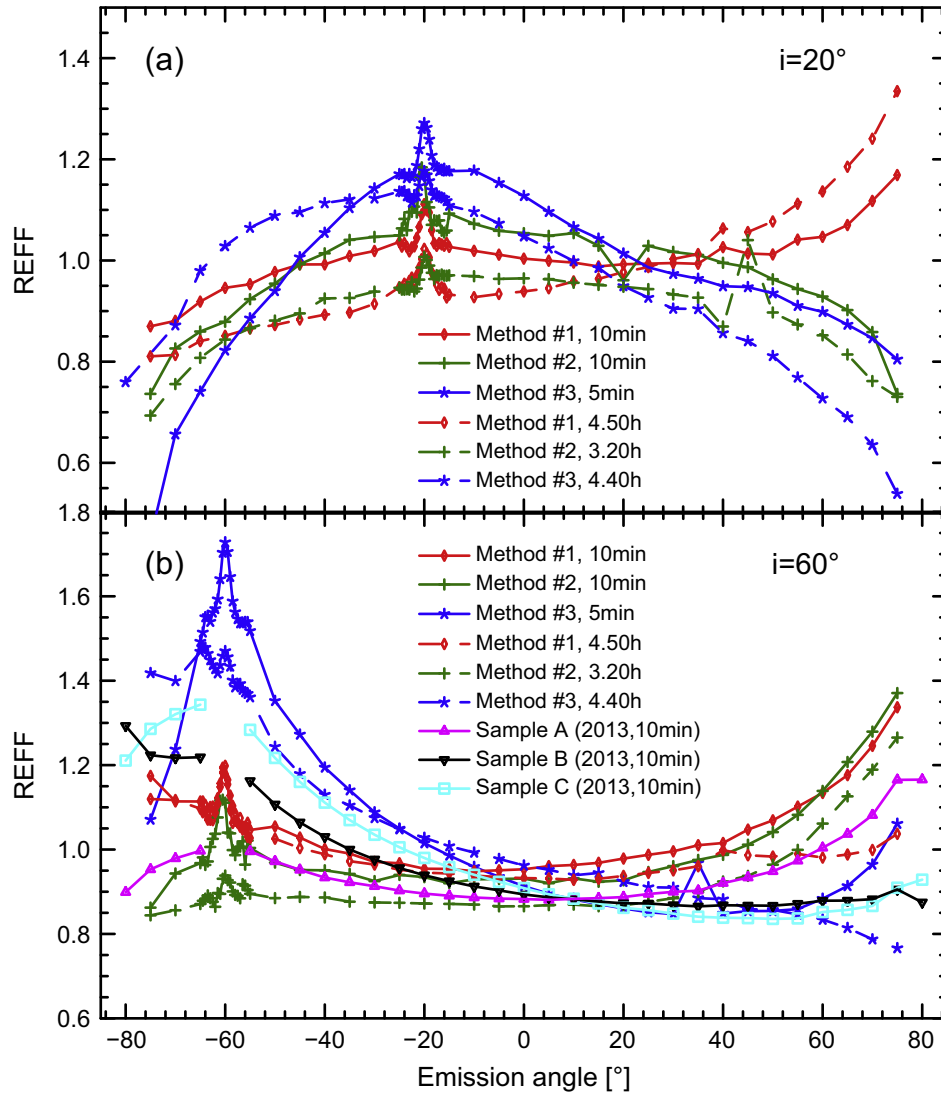


Fig. 14. Comparison of phase curves at incidence angles (a) $i = 20^\circ$ and (b) $i = 60^\circ$ for ice samples prepared with various methods, fresh and after a few hours. Sample A, B and C (plot b) are samples from our previous work and are compared to the new samples (Method #1, 2 and 3) prepared and measured in this article. All samples show a decrease in reflectance at small phase angles with time. At $i = 20^\circ$ the Method #2 sample originally scatters strongly in the forward direction but becomes even more forward scattering with time, while on the two samples which are initially backscattering (#1, #3) the forward fraction decreases. At $i = 60^\circ$, the 3 samples from our previous work all lie inside the range of curves measured with the new samples.

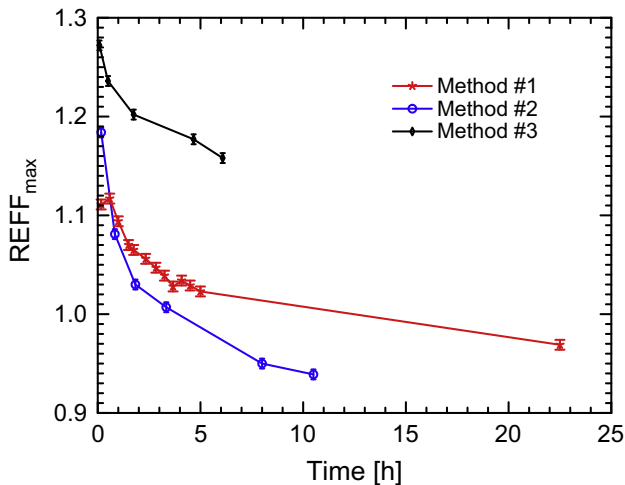


Fig. 15. Evolution of the maximum reflectance at opposition ($i = e = 0^\circ$) with time for the three ice samples. All samples show an exponential decrease of reflectance with time.

observed on the SEM images. This surface roughness favors multiple scattering and therefore hides the glory. Contrary to the opposition effect, for which particle size effects dominate the amplitude, the glory effect seems more sensitive to microscopic particle surface irregularities.

4.3. Possible applications of our results in remote sensing and future work

The observation of glory on laboratory ice surfaces provides an opportunity to deduce particle sizes and distributions directly from phase curves. As ice particles in the outer Solar System are expected to have similar sizes (e.g. A'Hearn et al., 2005; Sunshine et al., 2007; Dalton et al., 2012) it should be possible in theory to find glory effects in the Saturn E-ring or on the bright surfaces of Enceladus or Europa. Jaumann et al. (2008) analyzed the depth of the water absorption bands on Cassini/VIMS data and deduced particle diameters in the range of 10–30 μm over most regions, increasing with surface age. This range of particle size is exactly the one where glories can be observed in the visible spectrum of

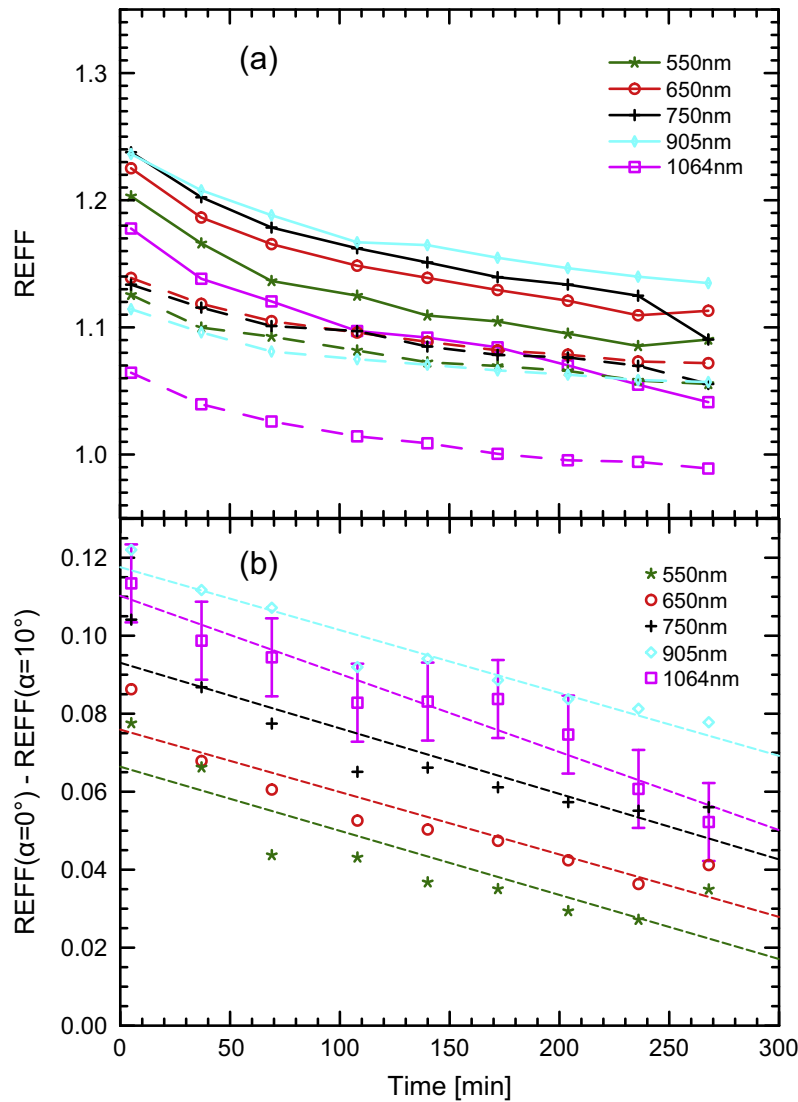


Fig. 16. (a) Reflectance factor, REFF, of ice prepared by Method #3 plotted as a function of time for different wavelengths. Solid lines: REFF at opposition ($i = 20^\circ, e = -20^\circ$). Dashed lines: REFF at a phase angle of 10° . The data plotted here are the same sequence as in Fig. 13. There is a continuous decrease with time of the reflectance at all wavelengths. However, the decrease with time of reflectance measured at opposition seems faster than the decrease of the reflectance at $\alpha = 10^\circ$. (b) Temporal evolution of the difference of reflectance between the opposition $\alpha = 0^\circ$ and at $\alpha = 10^\circ$, acting as an opposition amplitude definition. The dashed lines are linear fits per wavelength, the slope is almost identical except at 1064 nm, where it is a bit steeper. For the fresh sample, the opposition peak is about 60% higher at 905 nm than at 550 nm. The slightly reduced amplitude at 1064 nm compared to 905 nm is a hint of increased absorption at this wavelength. The general wavelength dependence is a strong indication for a significant contribution of the coherent backscattering to the opposition effect.

light. Since Kempf et al. (2010) showed in simulations that the deposition rate of ice particles ejected by plumes on Enceladus is quite high in some regions, one could assume that the morphology of particles is quite pristine and not dominated by effects such as sintering or space weathering. These environment conditions could potentially create and maintain surfaces made of spherical ice particles. Characterization of glories on the surface of icy moons by future space missions could be used as a complementary technique for grain size estimation. Because of the strong wavelength-dependence of this feature, visible color images at low phase angle would be ideal to invert information about the particle size distribution. Glories are also known to be strongly polarized (Laven, 2005a). Therefore, observation of the polarization of the reflected light could also be interesting to retrieve additional information about the properties of the scattering material.

The fact that the amplitude of the CBOE is dependent on wavelength and that CBOE has been observed on ice surfaces in the laboratory, which share many properties with icy material in

the outer Solar System, implies that the use of color filters in the VIS–NIR range on camera systems may provide additional information on future remote-sensing space missions. Further theoretical and experimental work will be required to better understand the relationships between the chemical and physical properties of the material and the shape and intensity of the opposition effect. Distinguishing the effects of the particle size and shape and the effect of sample roughness at larger scale seems quite challenging but would be very informative in the context of future planetary observations.

This question is particularly interesting in anticipation of the future measurements of the surface of Ganymede and Europa by optical instruments on ESA's JUICE mission (Grasset et al., 2012). The GAnymede Laser Altimeter (GALA) will accurately measure the topography of these two satellites, using laser ranging (Husmann et al., 2013). In addition to the topography, the Range Finder Module (RFM) adapted from BEpi-Colombo Laser Altimeter (BELA) instrument (Thomas et al., 2007) is also able to determine

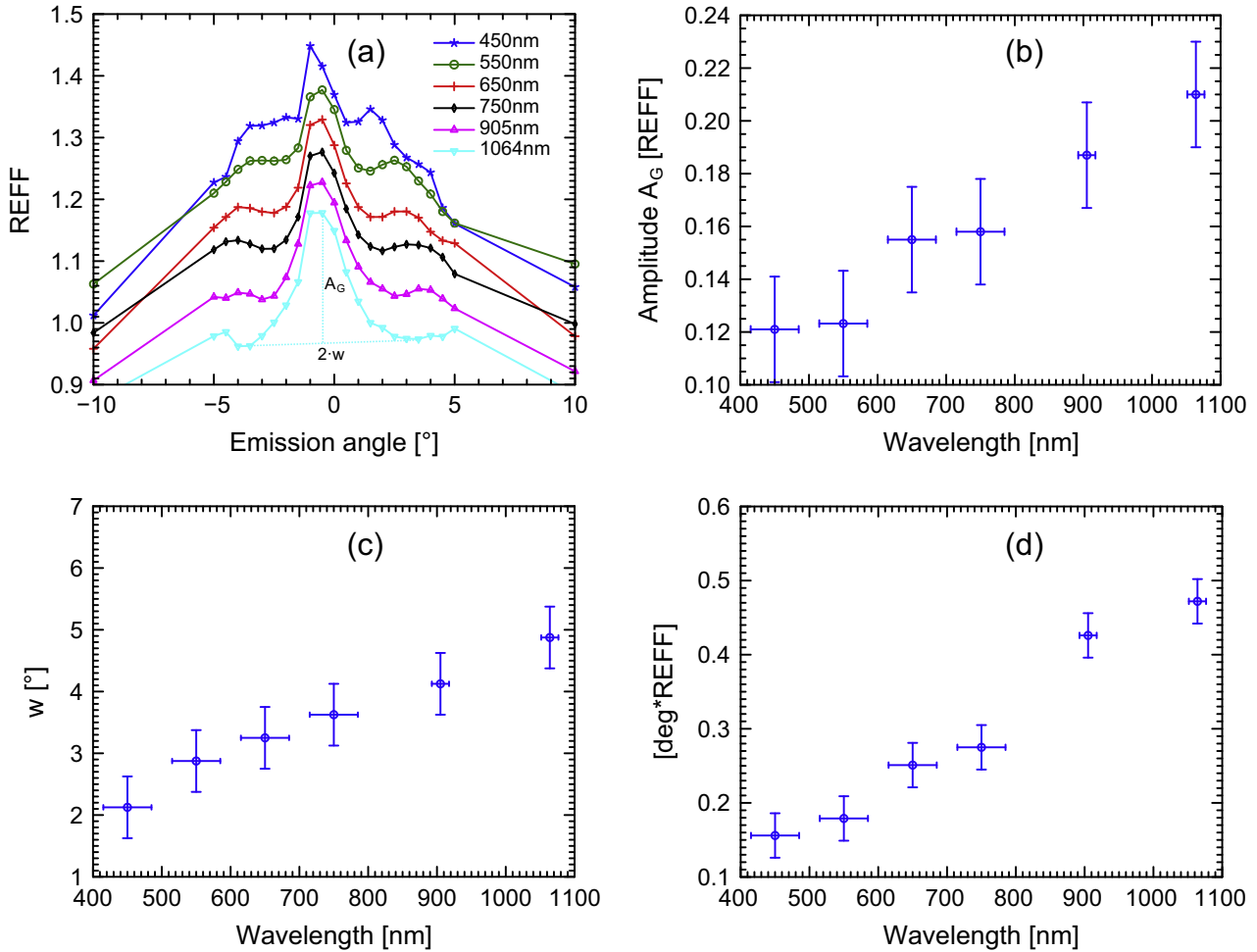


Fig. 17. (a) Phase curves of the Spheriglass 7025 sample measured at different wavelengths (zoom from Fig. 10a on the low phase angle region). The curves are shifted (-0.2 to $+0.1$) vertically to improve visibility. The local maxima attributed to glory are well visible in the range: $2^\circ < \alpha < 5^\circ$. The curve measured at 450 nm shows effect of the degraded signal noise ratio for this filter (1:30 compared to 750 nm). (b) shows the amplitude A_G of the central peak, and (c) the angular position of the local maxima of the glory as a function of wavelength. The nearly linear relationship observed is in agreement with the theory (see Fig. 18). (d) shows the integral of the central peak as a function of wavelength. The correlated change with wavelength of both, amplitude and angular width of the opposition peak, indicate that the opposition effect in this medium is mainly caused by coherent backscattering.

accurately the reflectance of the surface at the laser wavelength of 1064 nm. As, by principle, laser altimeters perform all measurements precisely in the opposition geometry, the reflectance that will be measured will potentially be largely affected by the CBOE. It is thus important to understand which parameters most influence the CBOE and how the observed variability of normal reflectance has to be interpreted.

In the future, we will also have to investigate whether coherent backscattering and glories are restricted to pure materials or can be observed as well when ice spheres are mixed with some fractions of other materials such as minerals and organics. This could have interesting implications for future high-resolution observations of cometary surfaces at low phase angle, such as the ones acquired by the OSIRIS camera system (Keller et al., 2007) onboard ESA's Rosetta mission.

In terms of hardware development, the use of polarizers on the PHIRE-2 goniometer can help to understand better the effects of coherent backscattering and distinguish them from shadow hiding effects.

5. Conclusion

The PHIRE-2 radio-goniometer has been in constant use since 2011 to measure the bidirectional reflectance of various types of

planetary analogs. The construction of a new sensor head equipped with a beam splitter is the most significant improvement to this instrument since its first measurements, as it now allows us to measure the reflectance of the sample at low phase angles. Despite the small size of the instrument and therefore a limited angular resolution, the results shown in this article prove that the measurements obtained can provide useful details on the opposition effect and its physical causes as well as on other particularly interesting features visible at low phase angles.

Measurements performed with this new setup ideally complement our previous work (Jost et al., 2013), in which we investigated the reflectance properties of surfaces made of micrometer-sized water ice particles. In addition to the new sensor head, the construction of a setup to produce this material at a faster rate and detailed characterization of the produced material in a cryo-SEM allows us to enrich both the measured reflectance dataset and our interpretations of the data. To complement our observations and test some of our hypotheses, we have acquired, in addition, similar measurements with well-characterized non-icy high albedo material.

We find that the reflectance of our ice samples in the opposition geometry is a very sensitive quantity, influenced by the size and shape of the particles as well as the porosity and the texture of the sample at larger scale. In addition, it shows a significant

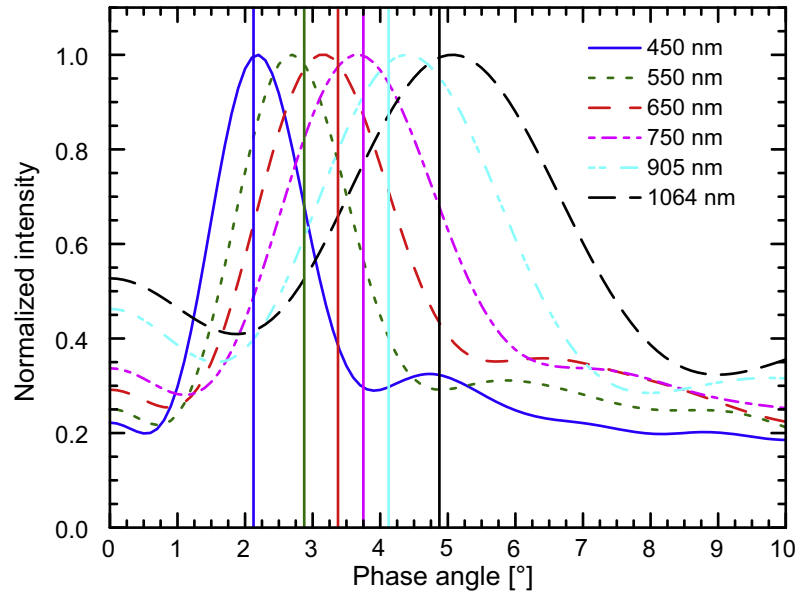


Fig. 18. Mie theory simulations of the glory effect for normal size distribution of Spheriglass particles ($\mu = 10 \mu\text{m}$, $\sigma = 20$) at different wavelengths. The refractive index is 1.51, as specified by Potter Industries. The vertical lines indicate the measured angular positions of the first maximum (Fig. 17).

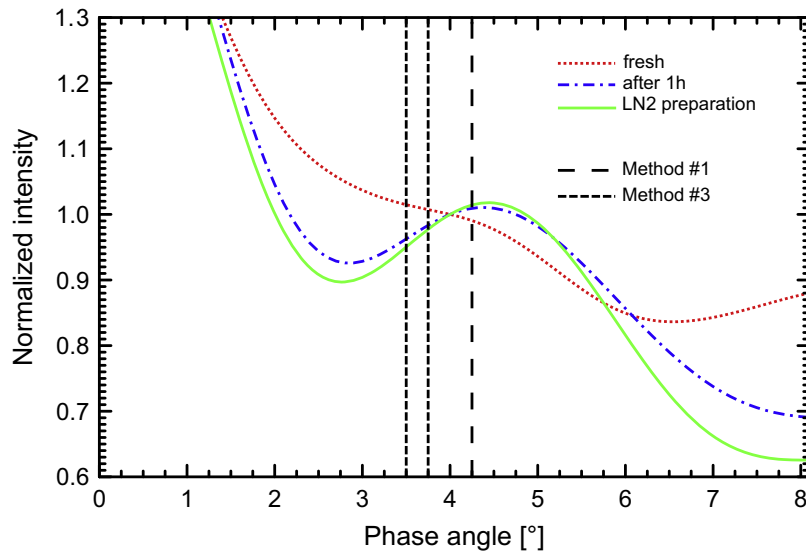


Fig. 19. Simulation of the glory effect on ice particles using Mie theory. The particle size distributions are obtained by the analysis of SEM images. The refractive index is 1.31 for water ice. Depending on the particle size distribution, the angular location of the first local maximum in the particle phase function shifts (smaller particles reduce the phase angle of the first maximum). The vertical black lines indicate the measured angular positions of the glory for samples prepared with Method #1 (long dashed) and with Method #3 (dashed). All phase curves are normalized at $\alpha = 4^\circ$. The measured angular positions show good agreement with the maxima of the simulated curves.

dependence on wavelength. The shape of the phase curve in the opposition region as well as its dependence on wavelength indicate the contribution of coherent backscattering to the Opposition Effect (CBOE). Around the central opposition peak, we observe on most ice samples a glory, which is a feature produced by the scattering of light scattering by spherical particles in the size range: 10–50 μm . These features are frequently encountered on terrestrial water clouds, but to our knowledge it is first time they are documented for surfaces made of ice particles in the laboratory.

These laboratory observations have important implications for future observations of outer Solar System icy surfaces. Because they show a strong dependence on the particle size and texture of the sample, they can provide insightful information on the physical properties of the surface material. As they are very sensitive to

wavelength and polarization, color imaging and polarization filters would be a useful addition to future camera systems. Besides cameras, the coherent backscattering will contribute significantly to the signal measured by laser altimeters acquiring data over icy satellites. The interpretation of the reflectance values and maps returned by such instruments would benefit from a good understanding of the influence of various physical parameters on the characteristics (intensity, angular width, shape) of the opposition surge.

Up to now, particle size estimation below the optical resolution from remote sensing was only possible by spectroscopy, where widths of absorptions bands are analyzed (see e.g. Hansen and Romain, 2012; Jaumann et al., 2008 in the case of Enceladus). The observation of glory on icy surfaces (e.g., on Enceladus, or

Europa) would provide the opportunity to estimate the particle size from visible remote-sensing as a complementary technique to infrared spectroscopy.

Acknowledgments

The construction of the facility was funded by the University of Bern and by the Swiss National Science Foundation, in particular through the R'equip grant # 206021_133827. We are grateful to all the engineers and technicians of the WP department at the University of Bern who participated in this project.

B. Gundlach is partly funded through DFG grant BL298/19-1 as a part of the Priority Program 1573 “Physics of the Interstellar Medium”.

Further we thank Philip Laven for the free supply of his MiePlot software.

We thank two anonymous reviewers for their constructive comments and suggestions.

References

- A'Hearn, M.F. et al., 2005. Deep impact: Excavating Comet Tempel 1. *Science* 310, 258–264.
- Akkermans, E., Wolf, P., Maynard, R., 1986. Coherent backscattering of light by disordered media: Analysis of the peak line shape. *Phys. Rev. Lett.* 56, 1471–1774.
- Allen, T., 1997. Particle Size Measurement, fifth ed. Chapman & Hall, ISBN 041272950.
- Belskaya, I. et al., 2008. Surface properties of Kuiper belt objects and centaurs from photometry and polarimetry. In: Barucci, M. et al. (Eds.), *The Solar System beyond Neptune*. The University of Arizona Press, Tucson, pp. 115–127.
- Benkhoff, J. et al., 1995. Energy analysis of porous water ice under space-simulated conditions: Results from the KOSI-8 experiment. *Planet. Space Sci.* 43, 353–361.
- Blackford, J.R., 2007. Sintering and microstructure of ice: A review. *J. Phys. D: Appl. Phys.* 40, R355–R385.
- Bobrov, M.S., 1970. Physical properties of Saturn's rings. In: Dollfus, A. (Ed.), *Surfaces and Interiors of Planets and Satellites*. Academic, New York, pp. 376–461.
- Brissault, O. et al., 2004. Spectrogonio radiometer for the study of the bidirectional reflectance and polarization functions of planetary surfaces. 1. Design and tests. *Appl. Opt.* 43, 1926–1937.
- Dalton, J., Shirley, J., Kamp, L., 2012. Europa's icy bright plains and dark lineae: Exogenic and endogenic contributions to composition and surface properties. *J. Geophys. Res.* 117, E03003.
- Déau, E. et al., 2013. Re-analysis of previous laboratory phase curves: 1. Variation of the opposition effect morphology with the textural properties, and an application to planetary surfaces. *Icarus* 226, 1465–1488.
- Deb, D. et al., 2011. The photometric study of light scattering from the surface of alumina powder and interpretations by Hapke formula. *Adv. Space Res.* 48, 1274–1278.
- Gardner, C.S., 1982. Target signatures for laser altimeters: An analysis. *Appl. Opt.* 21, 448–453.
- Grasset, O. et al., 2012. Jupiter Icy moons Explorer (JUICE): An ESA mission to orbit Ganymede and to characterise the Jupiter system. *Planet. Space Sci.* 78, 1–21.
- Gunderson, K., Thomas, N., 2008. Polarimetric NIR reflectance measurements of regolith simulants at zero phase angle. *Planet. Space Sci.* 56, 1925–1938.
- Gunderson, K., Thomas, N., Whitby, J.A., 2006. First measurements with the Physikalisches Institut Radiometric Experiment (PHIRE). *Planet. Space Sci.* 54, 1046–1056.
- Gunderson, K. et al., 2007. Visible/NIR photometric signatures of liquid water in martian regolith simulant. *Planet. Space Sci.* 55, 1272–1282.
- Gundlach, B., Blum, J., 2015. The stickiness of micrometer-sized water-ice particles. *Astrophys. J.* 798 (1), 12, article id. 34.
- Gundlach, B. et al., 2011. Micrometer-sized ice particles for planetary-science experiments – 1. Preparation, critical rolling friction force, and specific surface energy. *Icarus* 214, 717–723.
- Hansen, G.B., Romain, J., 2012. Modeling of layers of micron sized water ice over Enceladus surface to fit the 1–5 μm spectra from Cassini VIMS instrument. *Lunar Planet. Sci.* 43, Abstract #2625.
- Hapke, B., 1986. Bidirectional reflectance spectroscopy. IV – The extinction coefficient and the opposition effect. *Icarus* 67, 264–280.
- Hapke, B., 1993. *Theory of Reflectance and Emittance Spectroscopy: Topics in Remote Sensing*. Cambridge, UK.
- Hapke, B., 2002. Bidirectional reflectance spectroscopy: 5. The coherent backscatter Opposition Effect and anisotropic scattering. *Icarus* 157, 523–534.
- Hapke, B., van Horn, H., 1963. Photometric studies of complex surfaces with applications to the Moon. *J. Geophys. Res.* 68, 4545–4570.
- Hapke, B., Nelson, R., Smythe, W., 1998. The opposition effect of the Moon: Coherent backscatter and shadow hiding. *Icarus* 133, 89–97.
- Hapke, B. et al., 2009. A quantitative test of the ability of models based on the equation of radiative transfer to predict the bidirectional reflectance of a well-characterized medium. *Icarus* 199, 210–218.
- Hapke, B. et al., 2012. The wavelength dependence of the lunar phase curve as seen by the Lunar Reconnaissance Orbiter wide-angle camera. *J. Geophys. Res.* 117, E00H15. <http://dx.doi.org/10.1029/2011JE003916>.
- Helfenstein, P., Veverka, J., Hillier, J., 1997. The lunar opposition effect: A test of alternative models. *Icarus* 128, 2–14.
- Husmann, H. et al., 2013. The GAnymede Laser Altimeter (GALA) as part of the JUICE payload: Instrument, science objectives and expected performance. *EPSC* 2013 8, 428.
- Jaumann, R. et al., 2008. Distribution of icy particles across Enceladus' surface as derived from Cassini-VIMS measurements. *Icarus* 193, 407–419.
- Johnson, J.R. et al., 2006. Spectroscopic properties of material observed by Pancam on the Mars Exploration Rovers: 1. Spirit. *J. Geophys. Res.* 11, E02S14.
- Jost, B. et al., 2013. Micrometer-sized ice particles for planetary-science experiments – 2. Bidirectional reflectance. *Icarus* 225, 352–366.
- Kaasalainen, S., 2003. Laboratory photometry of planetary regolith analogs. 1. Effects of grain and packing properties on opposition effect. *Astron. Astrophys.* 409, 765–769.
- Kaasalainen, S., Muinonen, K., Piironen, J., 2001. Comparative study on opposition effect of icy Solar System objects. *J. Quant. Spectrosc. Radiat. Trans.* 70, 529–543.
- Kaasalainen, S. et al., 2002. Laboratory experiments on backscattering from regolith samples. *Appl. Opt.* 41, 4416–4420.
- Kaasalainen, S. et al., 2005. Small angle goniometry for backscattering measurements in the broadband spectrum. *Appl. Opt.* 44, 1485–1490.
- Keller, H.U. et al., 2007. OSIRIS: The scientific camera system onboard Rosetta. *Space Sci. Rev.* 128, 433–506.
- Kempf, S., Beckmann, U., Schmidt, J., 2010. How the Enceladus dust plume feeds Saturn's E ring. *Icarus* 206, 446–457.
- Kennedy, J., Eberhart, R.C., 1995. Particle Swarm Optimization. In: *Proceedings of IEEE International Conference on Neural Networks*, Piscataway, NJ, pp. 1942–1948.
- Laven, P., 2005a. Atmospheric glories: Simulations and observations. *Appl. Opt.* 44, 5667–5674.
- Laven, P., 2005b. How are glories formed? *Appl. Opt.* 44, 5675–5683.
- Li, J.-Y. et al., 2013. Global photometric properties of Asteroid (4) Vesta observed with Dawn Framing Camera. *Icarus* 226, 1252–1274.
- Liang, S., Mishchenko, M., 1997. Calculations of the soil hot-spot effect using the coherent backscattering theory. *Remote Sens. Environ.* 60, 163–173.
- Lumme, K., Irvine, W., 1976. Photometry of Saturn's rings. *Astron. J.* 81, 865–893.
- Markiewicz, W.J. et al., 2014. Glory on Venus cloud tops and the unknown UV absorber. *Icarus* 234, 200–203.
- Markwardt, C.B., 2008. In: Bohlender, D.A., Durand, D., Dowler, P. (Eds.), *Non-Linear Least Square Fitting in IDL with MPFIT*, vol. 441. Astronomical Society of the Pacific Conference Series, pp. 251–254.
- Mayer, B. et al., 2004. Remote sensing of water cloud droplet size distributions using the backscatter glory: A case study. *Atmos. Chem. Phys.* 4, 1255–1263.
- McEwen, A., 1991. Photometric functions for photoclinometry and other applications. *Icarus* 92, 298–311.
- McGuire, A., Hapke, B., 1995. An experimental study of light scattering by large irregular particles. *Icarus* 113, 134–155.
- Mie, G., 1908. Beiträge zur Optik trüber Medien, speziell kolloidaler Metallösungen. *Ann. Phys. (Leipzig)* 25, 377–452.
- Minnaert, M., 1941. The reciprocity principle in lunar photometry. *Astrophys. J.* 93, 403–410.
- Mishchenko, M., 1992. The angular width of the coherent back-scatter opposition effect: An application to icy outer planet satellites. *Astrophys. Space Sci.* 194, 327–333.
- Mishchenko, M., Travis, L., Lacis, A., 2006. *Multiple Scattering of Light by Particles*. Cambridge University Press, New York.
- Muinonen, K. et al., 2002. Asteroid photometric and polarimetric phase effects. In: Bottke, W. et al. (Eds.), *Asteroids III*. University of Arizona Press, Tucson, pp. 123–138.
- Muinonen, K. et al., 2012. Coherent backscattering verified numerically for a finite volume of spherical particles. *Astrophys. J.* 760 (2012), 118. <http://dx.doi.org/10.1088/0004-637X/760/2/118>.
- Müller, G., 1885. Resultate aus Helligkeitsmessungen des Planeten Saturn. *Astron. Nachr.* 110, 225–232.
- Näränen, J. et al., 2004. Laboratory photometry of planetary regolith analogs: 2. Surface roughness and extremes of packing density. *Astron. Astrophys.* 426, 1103–1109.
- Nelson, R.M. et al., 2000. The opposition effect in simulated planetary regoliths. Reflectance and circular polarization ratio change at small phase angle. *Icarus* 147, 545–558.
- Penttilä, A., 2013. Quasi-specular reflection from particulate media. *J. Quant. Spectrosc. Radiat. Trans.* 131, 130–137.
- Pommerol, A. et al., 2011. Photometry and bulk physical properties of Solar System surfaces icy analogs: The Planetary Ice Laboratory at University of Bern. *Planet. Space Sci.* 59, 1601–1612.
- Pommerol, A. et al., 2013. Photometric properties of Mars soil analogs. *J. Geophys. Res.* 118, 2045–2072.
- Psarev, V. et al., 2007. Photometry of particulate surface at extremely small phase angles. *J. Quant. Spectrosc. Radiat. Trans.* 106, 455–463.

- Rosenbush, V. et al., 2002. Photometric and polarimetric opposition phenomena exhibited by Solar System bodies. In: Videen, G., Kocifaj, M. (Eds.), *Optics of Cosmic Dust*. Kluwer Academic Publishers, Dordrecht, The Netherlands, pp. 191–224.
- Sears, D., Kochan, H., Huebner, W., 1999. Laboratory simulation of the physical processes occurring on and near the surfaces of comet nuclei. *Meteorit. Planet. Sci.* 34, 497–525.
- Seelinger, H., 1884. Zur Photometrie des Saturnrings. *Astron. Nachr.* 109, 305–316.
- Seelinger, H., 1887. Zur Theorie der Beleuchtung der grossen Planeten insbesondere des Saturns. *Abhandl. Bayer. Akad. Wiss. Math. – Naturvw.* KLII 16, 405–516.
- Shepard, M.K., Helfenstein, P., 2007. A test of the Hapke photometric model. *J. Geophys. Res.: Planets* 112 (11), E03001. <http://dx.doi.org/10.1029/2005JE002625>.
- Shkuratov, Y., Helfenstein, P., 2001. The opposition effect and the quasi-fractal structure of regolith: I. Theory. *Icarus* 152, 96–116.
- Shkuratov, Y. et al., 2002. The opposition effect and negative polarization of structural analogs for planetary regoliths. *Icarus* 159, 396–416.
- Souchon, A. et al., 2011. An experimental study of Hapke's modeling of natural granular surface samples. *Icarus* 215, 313–331.
- Sunshine, J.M. et al., 2007. The distribution of water ice in the interior of Comet Tempel 1. *Icarus* 190, 284–294.
- Thomas, N. et al., 2007. The BepiColombo Laser Altimeter (BELA): Concept and baseline design. *Planet. Space Sci.* 55, 1398–1413.
- Tsang, L., Ishimaru, A., 1985. Theory of backscattering enhancement of random discrete isotropic scatterers based on the summation of all ladder and cyclical terms. *J. Opt. Soc. Am. A* 2, 1331–1338.
- Van Albada, M., Van der Mark, M., Lagendijk, A., 1990. Experiments on weak localization of light and their interpretation. In: Sheng, P. (Ed.), *Scattering and Localization of Classical Waves in Random Media*. World Scientific, Teaneck, pp. 97–136.
- Verbiscer, A., Helfenstein, P., Veverka, J., 1990. Backscattering from frost on icy satellites in the outer Solar System. *Nature* 347, 162–164.
- Verbiscer, A., French, R.J., McGhee, C.A., 2005. The opposition surge of Enceladus: HST observations 338–1022 nm. *Icarus* 173, 66–83.
- Verbiscer, A., Helfenstein, P., Buratti, B., 2013. Photometric properties of Solar System ices. In: Gudipati, M., Castillo-Rogez, J. (Eds.), *The Science of Solar System Ices*. Astrophysics and Space Science Library 356, pp. 47–72.
- Warren, S., Brandt, R., 2008. Optical constants of ice from the ultraviolet to the microwave: A revised compilation. *J. Geophys. Res.* 113, D14220.
- Wolf, P.-E., Maret, G., 1985. Weak localization and coherent backscattering of photons in disordered media. *Phys. Rev. Lett.* 55, 2696–2699.
- Wolf, P.-E. et al., 1988. Optical coherent backscattering by random media: An experimental study. *J. Phys. France* 49, 63–75.